Mon. Not. R. Astron. Soc. **300,** 146–162 (1998)

Dark matter haloes within clusters

Sebastiano Ghigna,[1⋆] Ben Moore,[1] Fabio Governato,[1] George Lake,[2] Thomas Quinn[2] and Joachim Stadel[2]

[1]*Department of Physics, University of Durham, Durham DH1 3LE*
[2]*Department of Astronomy, University of Washington, Seattle, WA 98195, USA*

Accepted 1998 June 1. Received 1998 April 24; in original form 1998 January 21

ABSTRACT

We examine the properties of dark matter haloes within a rich galaxy cluster using a high-resolution simulation that captures the cosmological context of a cold dark matter universe. The mass and force resolution permit the resolution of 150 haloes with circular velocities larger than 80 $\mathrm{km\,s^{-1}}$ within the cluster virial radius of 2 Mpc (with Hubble constant $H_0 = 50\,\mathrm{km\,s^{-1}\,Mpc^{-1}}$). This enables an unprecedented study of the statistical properties of a large sample of dark matter haloes evolving in a dense environment. The cumulative fraction of mass attached to these haloes varies from close to zero per cent at 200 kpc to 13 per cent at the virial radius. Even at this resolution the overmerging problem persists; haloes that pass within 100–200 kpc of the cluster centre are tidally disrupted. Additional substructure is lost at earlier epochs within the massive progenitor haloes. The median ratio of apocentric to pericentric radii is 6:1, so that the orbital distribution is close to isotropic, circular orbits are rare and radial orbits are common. The orbits of haloes are unbiased with respect to both position within the cluster and the orbits of the smooth dark matter background, and no velocity bias is detected. The tidal radii of surviving haloes are generally well-fitted using the simple analytic prediction applied to their orbital pericentres. Haloes within clusters have higher concentrations than those in the field. Within the cluster, halo density profiles can be modified by tidal forces and individual encounters with other haloes that cause significant mass loss – 'galaxy harassment'. Mergers between haloes do not occur inside the cluster virial radius.

Key words: methods: numerical – galaxies: clusters: general – galaxies: haloes – cosmology: theory – dark matter – large-scale structure of Universe.

1 INTRODUCTION

Rich clusters of galaxies are large cosmological laboratories that may provide unbiased mixtures of the matter content of the Universe (White et al. 1993; Evrard 1997). Clusters are prominent structures in the Universe; their evolution can be followed with samples out to $z \sim 1$ (Rosati et al. 1998). They are the most massive virialized objects in the Universe and are the most recent objects to form in hierarchical formation models. Their masses can be determined by several independent methods (e.g. Carlberg et al. 1997b; Cen 1997; Wu & Fang 1997; Smail et al. 1997).

The evolution of the mass function of clusters is sensitive to key cosmological parameters (e.g. Bahcall, Fan & Cen 1997; Bartelmann et al. 1998; Borgani et al. 1997a; Carlberg et al. 1996; Eke, Cole & Frenk 1996; Wilson, Cole & Frenk 1996). This evolution can be calculated by using either analytic methods (Press & Schechter 1974) or cosmological *N*-body simulations (Eke, Navarro & Frenk 1997). The weakness of analytic methods is their inability to follow haloes that accrete into larger systems. In the past, numerical simulations have shared this problem. To sample a large volume, the poor resolution within virialized systems leads to soft, diffuse haloes that are rapidly dissolved by tidal forces. This is the classic overmerging problem (White et al. 1987) that has led to problems when comparing the mass distribution within dark matter simulations with the observed properties of galaxies (Summers, Davis & Evrard 1995).

We were determined to perform simulations that resolved the distribution and evolution of galaxy haloes within clusters. There are many questions that we will address with these simulations. What is the orbital distribution of the galaxies within clusters and are they biased in any way? What is the extent of galactic dark haloes within clusters and how much of the mass distribution of the cluster is attached to galaxies? How do these properties evolve with time and within different cosmological models? Are the density profiles of isolated 'field' haloes similar to the haloes that form within the environment of a rich cluster? How does the cluster environment modify the internal structure of haloes? The frequency of mergers between haloes within the cluster environment and the

⋆ E-mail: S.S.Ghigna@durham.ac.uk

heating rate from halo–halo encounters are questions of importance for studies of the morphological evolution of clusters. These are amongst the many questions that have remained unanswered due to the overmerging problem.

Some have suggested that the only way to avoid overmerging is to follow the evolution of the baryons, even if they are only ∼5 per cent of the mass (Evrard, Summers & Davis 1994). This assertion seems counter-intuitive; it is now clear that mass and force resolution can overcome the overmerging problem in dark matter simulations (cf. Moore, Katz & Lake 1996; Klypin, Gottlöber & Kravtsov 1997; Brainerd, Goldberg & Villumsen 1998; Moore et al. 1998). With fast parallel computers and highly tuned algorithms, our simulations have hundreds of surviving haloes within the virial radius of a rich cluster (Moore et al. 1998). Increased mass and force resolution lead to higher central densities in galactic haloes, enabling greater survival within a cluster. For the first time we can compare the mass distribution with the galaxy distribution in a rich cluster. Note that the loss of DM substructure can also be a physical effect; similar-mass mergers during the assembling of the cluster will lead to a single halo with no memory of its history.

The plan of this paper is as follows: In Section 2, we describe the *N*-body simulation, techniques and parameters. In Section 3 we describe two algorithms to identify 'haloes within haloes'. After creating a catalogue of haloes, Section 4 turns to results on their global properties: sizes, masses, radial distribution, orbital properties and merger histories. Section 5 discusses the internal properties of haloes: their density profiles, correlations between structure parameters and global parameters and the evolution of these quantities with time. We conclude in Section 6.

2 THE *N*-BODY SIMULATION

One of the goals of performing cosmological numerical simulations is to compare the distribution and bulk properties of dark matter with the distribution and properties of the observable galaxies. A direct comparison has never been possible, since structure in high-density regions has been quickly erased as a consequence of numerical resolution – the overmerging problem. 'Galaxies' are typically selected from the mass distribution in a cosmological simulation using a biased sample of dark matter particles. Previous studies of cluster substructure have been limited to using 'galaxy tracers' (Carlberg 1994; Summers et al. 1995), such as following the most bound particle of a halo before it becomes disrupted by the tidal field of the system. These hueristics enable the use of low-resolution simulations, but their validity is anyone's guess at this point (Summers et al. 1995).

There are now several codes that are able to simulate a gaseous component. Although these codes are invaluable for many astrophysical problems, the original motivation behind these techniques was the hope of resolving galaxies in a cosmological context, thus solving the overmerging problem. They hoped to form galaxies and preserve them by increasing the central densities owing to gas dynamics. In turn, the haloes would be more robust to disruption. Indeed, SPH simulations of individual clusters do give rise to a set of galaxy tracers that resemble a 'real' cluster. However, the mass resolution in the dark matter component is not sufficient to resolve the dark haloes of the galaxy tracers, so typically one is left with a cold gas blob orbiting within the smooth cluster background (Frenk et al. 1996). There are a variety of pathologies that arise if one uses too few particles to simulate a large dynamic range in scales. Our simulations are designed to resolve scales of 5 kpc using dark matter. This would be a minimal resolution to simulate galaxy formation with gas dynamics. One needs a fiducial dark matter simulation at high resolution to see differences owing to gas dynamics. One must ensure that these differences are sensible as an external check. With the gas representing $\lesssim$10 per cent of the mass, gross changes in numbers and orbits of galaxies would be surprising.

Our aim is to achieve very high spatial and mass resolution within a rich virialized cluster drawn from a 'fair volume' of 100 Mpc^3 in a standard CDM universe. In such a volume, there are several rich clusters, and none dominates the environment in an undesirable way. Any simulation method limits the number of particles that can be used in a single simulation. Previous simulations of clusters suffered limitations due to the small volume used, forcing the run to stop at $z \sim 1$ (Evrard et al. 1994) or or the use of vacuum boundary conditions outside the cluster (Carlberg 1994).

With current technology, we can perform a single large simulation of $\sim 10^8$ particles or try to tackle a number of different problems using simulations with $\sim 10^7$ particles. If we simulate our 'fair volume' at uniform resolution, there will be $\sim 10^4$ particles within the virial radius of a cluster, a resolution that is insufficient to resolve substructure. Previous attempts to resolve the inner structures of cluster haloes using $\sim 10^5$ particles failed to resolve more than a handful of satellite haloes (Carlberg 1994; Carlberg & Dubinski 1991; Tormen 1997; Tormen, Diaferio & Syer 1998). To achieve higher resolution within an individual cluster we initially perform a simulation of a large volume of a CDM universe as described above, normalized such that $\sigma_8 = 0.7$ and the shape parameter $\Gamma = 0.5$ ($H = 50\,\mathrm{km\,s^{-1}\,Mpc^{-1}}$ is adopted throughout).

We used a nesting scheme that we call 'volume renormalization' to achieve higher resolution within a region of greater interest. This technique has been used to probe quasar formation at high redshift (Katz et al. 1994) and to follow the density profiles of haloes in a cosmological context (Navarro, Frenk & White 1996). We generate initial conditions (ICs) for the volume at two resolutions, one that places $\sim 10^7$ particles within the entire volume and one such that there would be $\lesssim 10^6$ particles in the targetted cluster. We run the lower resolution model and select a virialized cluster at $z = 0$. The particles within about twice the virial radius of the cluster in the final state are traced back to their locations in the ICs. Within this region, we use the higher resolution ICs. Beyond this high-resolution region the mass resolution is decreased in a series of shells by combining particles in the high-resolution ICs at their centre of masses. In this way, the external tidal field is modelled correctly. The starting redshift in the high-resolution run is increased to $z = 69$ such that the perturbations in the smoothed density field of the high-resolution region obey the constraint $\delta\rho/\rho < 0.1$. We then re-run the simulation to the present epoch.

We use a new high performance parallel treecode PKDGRAV to evolve the particle distribution. PKDGRAV has accurate periodic boundaries and an open-ended variable time-step criterion based upon the local acceleration (Quinn et al. 1997). The code uses a spline softening length such that the force is completely Newtonian at twice our quoted softening lengths. In terms of where the force is 50 per cent of the Newtonian force, the equivalent Plummer softening length would be 0.67 times the spline softening length. In the high-resolution region, our particle mass is $8.6 \times 10^8\ \mathrm{M}_\odot$. We perform two runs with 10 kpc (RUN1) and 5 kpc (RUN2) softening lengths. The final virial radius of the cluster is ∼2 Mpc and the mass is $4.6 \times 10^{14}\ \mathrm{M}_\odot$ so that we have approximately 600,000 particles within a sphere of overdensity 200. (Note that the cluster that is analysed here is the 'Virgo' cluster from Moore et al. 1998.)

We have analysed both simulations and present results for each run, except when this would lead to duplication of plots or text without any gain in information. In these cases, we follow the policy of showing results for RUN2 when haloes are used as tracers, and RUN1 when we also require information on their internal structure. This is because RUN2 has better spatial resolution but the same mass resolution as RUN1, although the softening length used in RUN1 will help suppress two-body relaxation effects and yield less noisy profiles of small haloes. (With hindsight, this caution appears to be superfluous.)

3 CLUSTER SUBSTRUCTURE AND HALO IDENTIFICATION

3.1 The density distribution in the cluster

In past work, haloes in dissipationless *N*-body simulations have usually spontaneously dissolved when entering clusters. Two physical effects conspire with the finite numerical resolution to erase dark matter haloes in clusters (Moore, Katz & Lake 1996). Halos are heated by cluster tides and halo–halo encounters, thus losing mass as they move into the potential well. (In the following, 'tidal disruption' refers to the sum of these effects, unless we excplicitly state otherwise.) When the halo radius approaches ∼3 times the 'core radius' (owing to either a density plateau or gravitational softening), the halo dissolves. Hence, it takes very high resolution to retain dark matter substructures at a distance 100–200 kpc from the centre of a cluster. Our numerical parameters were chosen so that haloes would survive at these scales. The wealth of haloes retained in our simulated cluster is visible in Fig. 1

The upper panel is a map of the density distribution in a box of size R_{200} (see Section 3.2 for a precise definition), centred on the cluster and projected on to a plane. Each particle is plotted using a grey-scale according to the logarithm of the local density [defined using an SPH smoothing kernel over 64 particles in a code called SMOOTH (Stadel & Quinn 1997, http ref: http://www-hpcc.astro.washington.edu/tools)]. Only regions with density contrast $\delta > 30$ are shown. The cluster boundaries, set at R_{200}, correspond to the con tours of the central bright region. Much of the mass inside R_{200} lies in the dark matter haloes that we will analyse here. Their projected distribution is shown as a 'circle plot' in the lower panel of Fig. 1. The radius of each circle is the halo radius (Section 3.3) in units of R_{200}. Note that haloes of similar central densities (similar brightness in the density map) may have largely different radii depending on their distances from the centre of the cluster. It is remarkable that substructure haloes cover such a large fraction of the projected cluster area. Comparing the two panels of Fig. 1, we note that the density map gives an excessive impression of overmerging within the central parts of the cluster with respect to the actual projected distribution of the haloes.

3.2 Cluster properties and evolution

We define the cluster centre as the position of its most bound particle. This particle is within a softening length of the centre of the most massive halo found by SKID (see Section 3.3). The density profile of the RUN1 cluster calculated in spherical shells is shown in the upper panel of Fig. 2 (the solid line is for $z = 0$ and dotted line for $z = 0.5$). The cluster forms at $z \sim 0.8$ from the mergers of many haloes along a filamentary structure and at $z = 0.5$ it has not yet virialized since it still has quite a lumpy structure, but the global density profile is roughly similar to that measured 5 Gyr later at

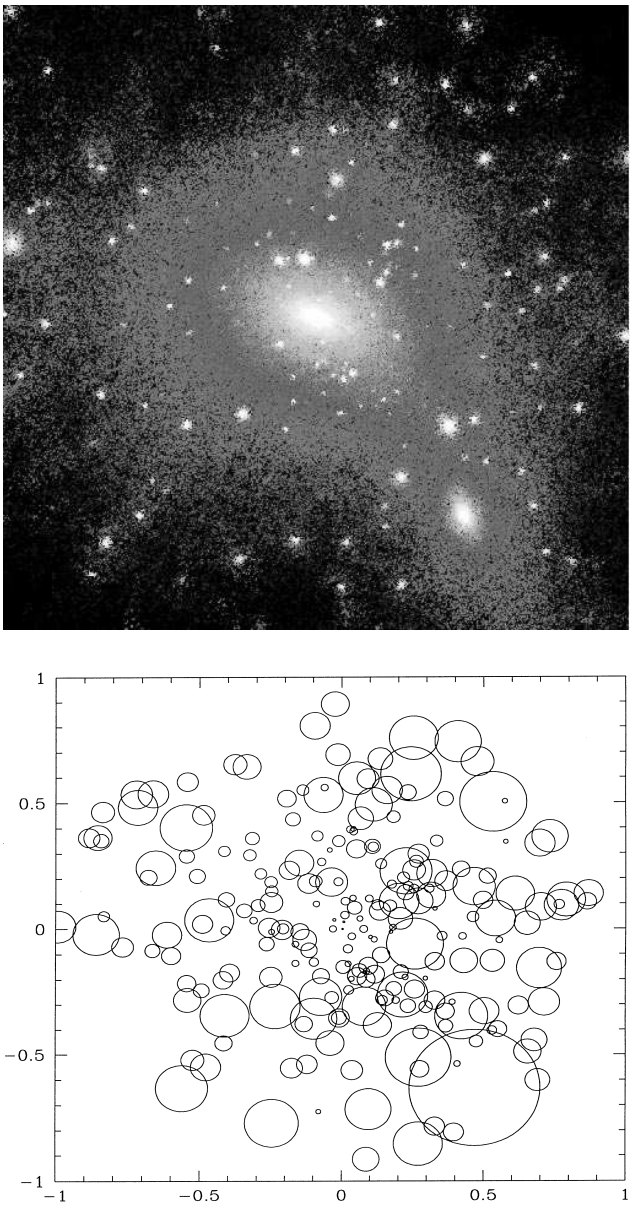

Figure 1. Density map (upper panel) and circle plot of the halo radii within the virial radius of the cluster (taken here as the length unit) at $z = 0$. (The density map is the projection of the mass in a box and contains a few haloes at the periphery of the clsuter that do not appear in the circle plot.)

$z = 0$. (We shall compare properties of the substructure identified at both epochs.)

The lower panel of this figure shows the circular velocity profile $V_c(R) \equiv [GM(R)/R]^{1/2}$, where $M(R)$ is the mass within R. The virial radius of the cluster is defined as the distance R_{200} for which the average density enclosed, $\bar{\rho}_C(R_{200})$, is 200 times the cosmic density, ρ_{cr}; we obtain $R_{200} = 1.95$ Mpc at $z = 0$ and 1.2 Mpc at $z = 0.5$. The cluster is not spherical and has axial ratios that are roughly 2:1:1. (In the following we will always use units of kpc and km s^{-1} for lengths and velocities, unless we explicitly state otherwise.)

Fig. 3 shows the growth of the cluster mass with redshift. Defining the formation redshift of the cluster as that where it has accreted half of its final mass, $z_{form} \sim 0.8$ for our cluster. This is slightly earlier than expected for an average cluster of this mass from the Press–Schechter theory (Press & Schechter 1974; Lacey &

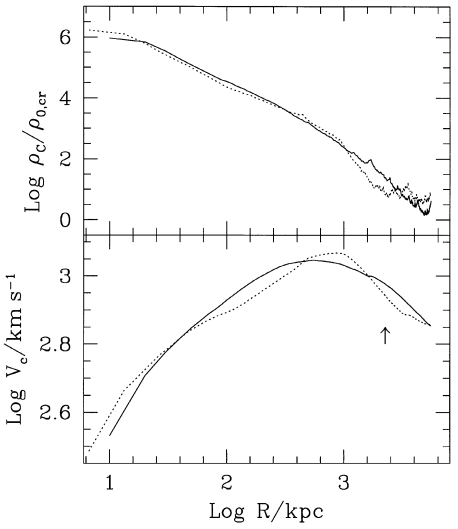

Figure 2. The density (upper panel) and circular velocity (lower panel) profiles for the cluster. The solid curves are at the final epoch and the dotted curves show the cluster at a redshift $z = 0.5$. The density is measured in units of the present critical density $\rho_{0,cr}$; R is the physical distance to the cluster centre, and was set at the location of the most bound particle. The arrow marks the value of the cluster virial radius R_{200} at $z = 0$.

Cole 1993), where $z_{form} \sim 0.5$ (as calculated from a routine kindly supplied by Paolo Tozzi). This is not an unwelcome feature, since the cluster is in true virial equilibrium at $z = 0$.

3.3 Halo identification

Identifying dark matter (DM) haloes in the high-density environment of the cluster is a critical step (cf. Klypin, Gottlöber & Kravtsov 1997). The haloes jump out visually, so while it is relatively straightforward to identify the halo centres, we must select only the bound particles to characterize the halo. We want to screen the cluster background that is streaming through, but the substructure itself will be tidally distorted and may have tidal tails of material that are loosely attached to the halo. Our group-finding algorithm uses local density maxima to find group centres and and then iteratively checks for self-boundedness to define group membership. Each *group* of particles found belongs to an individual *halo*. The algorithm is an improved version of DENMAX, named SKID, and is fully described by Stadel et al. (1996, see http ref: http://www-hpcc.astro.washington.edu/tools). For each simulation we adopt a linking length of $1.5l_{soft}$ and a minimum number of member particles of 16, corresponding to a mass of $\simeq 1.35 \times 10^{10}$ M$_\odot$. In general, we shall use haloes with more than 16 particles when they are employed as tracers, but we shall adopt a minimum number of 32 particles when their individual properties are relevant.

The high-resolution region that we analyse is roughly the turn-around radius of the cluster or about twice the virial radius, $R_{ta} \simeq 2R_{200} \simeq 5$ Mpc. Within this radius, there are 495 and 522 haloes for RUN1 and RUN2, and 208 and 227 haloes respectively within R_{200}. Changing l_{soft} by a factor of 2 does not make much difference on a global scale, but if we restrict ourselves to the inner parts of the cluster the difference between the numbers of haloes changes significantly: inside $R < R_{200}/2$, RUN2 has 91 haloes compared with the 59 found in RUN1, and RUN2 has twice as many within $R < R_{200}/4$ (30 instead of 16). The innermost haloes in RUN1, and RUN2 are at $\sim$200 kpc and $\sim$100 kpc respectively. These differences reflect the effect of the softening length on the central densities of the haloes that determine their survival against tidal disruption (Moore et al. 1998; see also the discussion related to Fig. 5 later). Quality control of our halo-finding algorithm was ensured by visually inspecting the density distribution inside R_{200} to verify that we neither missed nor created structures.

We use the output of SKID to determine the halo structural parameters. In particular, it estimates the extent of a halo using

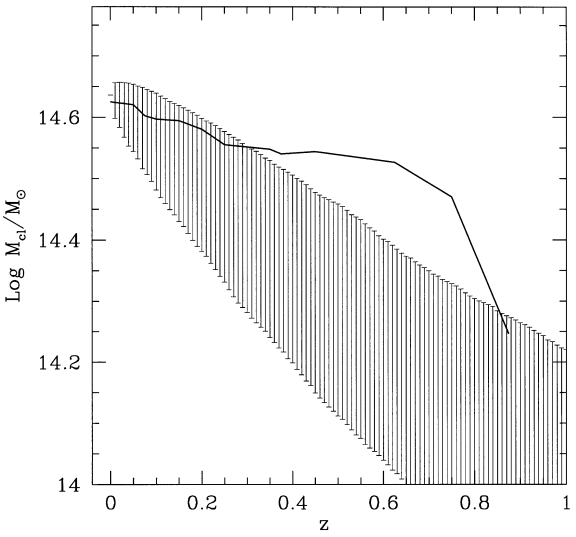

Figure 3. Growth of the mass of the cluster M_{cl} with redshift z. M_{cl} is the mass encompassed by the 'virial' radius of the cluster at each z. The error bars delimit the 1σ confidence interval for the growth rate predicted using the Press–Schechter theory.

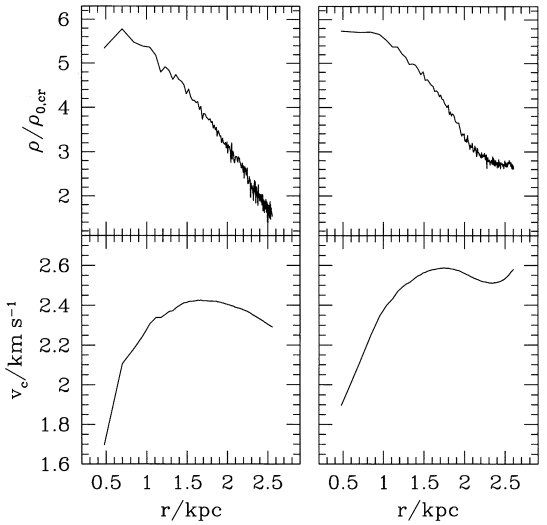

Figure 4. Density profiles and circular velocity profiles are plotted for two large dark matter haloes extracted from the simulation. The left panel is a 'peripheral' halo that lies beyond the main virial radius of the cluster at $R = 4.2$ Mpc. The halo in the right panel lies within the cluster at $r = 1.2$ Mpc. The radius r measures the distance from the centre of each halo. In the latter case, the radius at which the high-density background of cluster particles dominates the halo particle distribution is apparent as a flattening of $\rho(r)$ and the linear rise of $v_c(r)$ in the outer regions. We denote the peak value of the circular velocity as v_{peak} and the radius at which it occurs as r_{peak}.

the distance to the least bound particle. However, the full six-dimensional phase space information is never available in the real Universe, therefore we shall compare results from SKID using an 'observable' quantity for each halo. For example, the (projected) mass distributions can be determined using either weak lensing, the rotation curves of spirals or the velocity dispersion profiles of ellipticals. Motivated by gravitational lensing, one possibility is to define the radius of a halo using its density profile $\rho(r)$, where r is the distance from the centre of the halo, and measuring the radius ($\equiv r_\rho$) at which the local density of the cluster background dominates and $\rho(r)$ flattens (cf. Fig. 4). Rotation curves or velocity dispersion profiles of isolated objects will eventually decline with radius, but if a halo is embedded within a deeper potential, at some radius its profile will turn around and increase as the velocity dispersion of the cluster background starts dominating. (Fig. 4, right panels, shows that the positions of these inflexion points are essentially equal.) We therefore combine these two definitions and use the inflexion point ($\equiv r_{\rm vc}$) of the effective circular velocity $v_{\rm c} = [GM(r)/r]^{1/2}$ as an alternative independent estimate of the extent of a halo (cf. Fig. 4).

The circular velocity is less noisy than the density or velocity dispersion and thereby more suitable for an automated procedure. Moreover, the inflexion point of $v_{\rm c}(r)$ can be easily detected by searching for a minimum, without any knowledge of the background density (as would be necessary if we were to implement an overdensity criterion). The radius $r_{\rm vc}$ can either overestimate r_ρ for steeply declining velocity profiles, or underestimate it for profiles close to isothermal. If the haloes are described by the NFW model (Navarro et al. 1996; see also Section 5), the former condition applies to haloes with $v_{\rm c} \sim 50\,{\rm km\,s^{-1}}$ and the latter to haloes with $v_{\rm c} \gtrsim 200\,{\rm km\,s^{-1}}$ for background densities ~ 300 times the cosmic average (as we will see, however, the profiles of tidally 'stripped' haloes decline with r more steeply than an NFW profile). In our case, for small haloes, the difference can be at most $\sim$10 per cent; as for large haloes, $r_{\rm vc}$ differs from r_ρ by $\lesssim$20 per cent in about one-third of the haloes in our sample with $v_{\rm c} \gtrsim 120\,{\rm km\,s^{-1}}$. These differences do not significantly affect our results. With this definition, there is a contribution to the mass encompassed by a halo from the smooth background of order 20 per cent, which we subtract from the quoted halo masses.

For each SKID halo, we calculate $\rho(r)$ and $v_{\rm c}(r)$ using equally spaced bins of 2 kpc, such that the number of particles in each bin is nearly equal. The departure of $\rho(r)$ from isothermality is betrayed by a peak of $v_{\rm c}(r)$, $v_{\rm peak}$, occurring at $r_{\rm peak}$. The catalogue values of $r_{\rm pk}$ and $v_{\rm pk}$ are estimated by fitting a cubic spline to $v_{\rm c}(r)$. The left panels of Fig. 4 show sample $\rho(r)/\rho_{0,\rm cr}$ and $v_{\rm c}(r)$ curves for a large *peripheral halo* at a distance of $R = 4.2$ Mpc from the centre of RUN1 (hereafter *cluster haloes* are those within R_{200}, and *peripheral haloes* those between R_{200} and $R_{\rm ta}$).

Haloes beyond the cluster boundary can be easily characterized by their 'virial' radii and masses $M_{200} \equiv M(r_{200})$. For isothermal spheres the circular velocity at r_{200} is $v_{200} = (r_{200}/\,{\rm kpc})h\,{\rm km\,s^{-1}}$ to within a few per cent. For the halo mentioned above, $r_{200} \simeq 400$ kpc ($M_{200} = 3.4 \times 10^{12}\,{\rm M_\odot}$). The right panels of Fig. 4 show $\rho(r)/\rho_{0,\rm cr}$ and $v_{\rm c}(r)$ for a tidally limited massive cluster halo at $R = 1.2$ Mpc, where $\rho_{\rm bkg} \simeq 300\rho_{0,\rm cr}$. The halo radius $r_{\rm halo}$ is either the virial radius, r_{200}, or the *tidal radius*, $r_{\rm tid}$, as appropriate. Similarly, the halo mass is defined as $M_{\rm halo} \equiv M(r_{\rm halo}) = v_{\rm c}(r_{\rm halo})^2 r_{\rm halo}/G$.

Force softening and the finite mass resolution introduce halo *cores* that are visible in Fig. 4 as a flattening of $\rho(r)$ at $r \lesssim 10$ kpc. We define a *core radius* $r_{\rm core}$ for each halo as the radius where $v_{\rm c}$ has risen to 70 per cent of $v_{\rm peak}$.

Once the halo positions and structural parameters are known, we can start to address the questions raised in the Introduction. We begin by examining the global properties of the halo distribution, with a preliminary discussion of numerical resolution effects.

4 PROPERTIES OF THE HALO DISTRIBUTION

4.1 Numerical resolution effects

Halo in clusters are 'harassed' by encounters with other haloes combined with strong global tides. This adds internal energy and leads to mass loss. Using a static cluster potential, Moore, Katz & Lake (1996) found that haloes rapidly disrupt when $r_{\rm tid} < 3$–$4r_{\rm core}$. Our fully self-consistent simulations verify this. Fig. 5 shows the ratios $r_{\rm core}/r_{\rm halo}$ versus R for our halo set using RUN1. This ratio increases towards the cluster centre and no haloes exist with $r_{\rm core}/r_{\rm halo} \gtrsim 0.3$. (Similar results hold for RUN2.) Clearly, the softening will set a floor to the core radius, but in general we find that $r_{\rm core} \sim l_{\rm soft}$, and correspondingly that haloes smaller than $\sim 3l_{\rm soft}$ have all dissolved. The lower boundary for $r_{\rm halo}$ in RUN1 and RUN2 is indeed $\sim$30 and $\sim$15 kpc respectively.

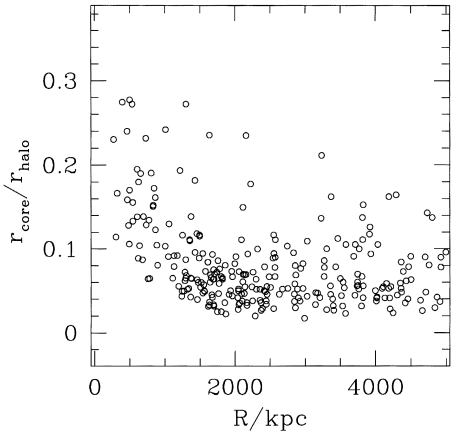

Figure 5. For every halo within $R = 5$ Mpc we plot the ratio of halo core radii and outer radii versus clustercentric position. Halos contain at least 32 particles.

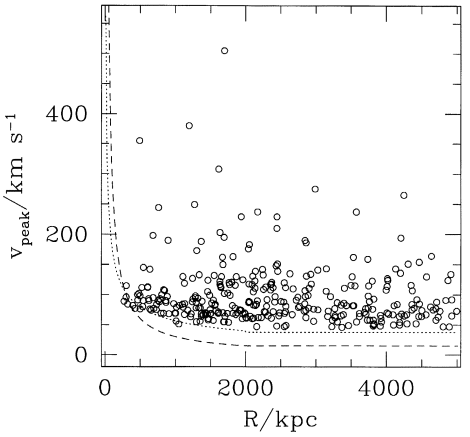

Figure 6. The peak circular velocity of haloes, $v_{\rm peak}$, is plotted against their clustercentric position R at $z = 0$. The lines give the expected limiting R at which haloes of given $v_{\rm peak}$ can be resolved because of the finite spatial resolution (dashed curve) and mass resolution (dotted line).

Numerical limitations can also be seen in Fig. 6, a plot of $v_{\rm peak}$ versus R for RUN1. There is no bias apparent in this plot; haloes of all circular velocity exist over a wide range in R. We show two curves that exclude regions of space owing to our numerical resolution: (i) defining a minimum particle number to identify haloes sets a lower mass limit, $M_{\rm lim} = 1.35 \times 10^{10}\,{\rm M}_{\odot}$, and (ii) $r_{\rm tid}$ is correlated with R and haloes dissolve when $r_{\rm tid} \gtrsim 3r_{\rm core} \simeq 3l_{\rm soft}$. Approximating the haloes as isothermal spheres that are tidally stripped like layers off an onion, the mass and circular velocity are related as $M_{\rm halo} \equiv M_{200} = Gv_{\rm c}^2 r_{200}$ for unstripped peripheral haloes and $M_{\rm halo} \simeq Gv_{\rm c}^2 r_{\rm tid}$ for 'stripped' cluster haloes. The tidal radius of a halo can also be obtained from $v_{\rm c}$ through $r_{\rm tid} \simeq Rv_{\rm c}/V_{\rm c}$ ($V_{\rm c} \simeq 1000\,{\rm km\,s^{-1}}$ is the circular velocity for the cluster) in the approximation that a halo at R is tidally truncated 'locally', i.e. according to the value of $\bar{\rho}_{\rm C}$ at R (this is a limiting case as their pericentric radius can only be smaller). Applying condition (i) leads to the dotted line in Fig. 6; criterion (ii) leads to the dashed line (we set $v_{\rm c} = {\rm constant} = v_{\rm peak}$). If tides due to the cluster potential are the only cause of halo disruption, our sample should be complete for haloes with $v_{\rm peak} \gtrsim 80\,{\rm km\,s^{-1}}$ and pericentres that have always been greater than $R_{\rm lim} \sim 250\,{\rm kpc}$. (Isolated dark matter haloes in N-body simulations are better described by NFW profiles – see Section 5 – than by isothermal profiles; however, the differences between the two are not significant for the bulk of the cluster haloes, the profiles of which do not extend to their virial radii and are 'resolved' to the level of ∼300–400 particles. For this reason, using the isothermal model is a sufficient and simple way of interpreting our results.)

4.2 Spatial distribution of haloes

The number density of haloes, $n_{\rm haloes}$, is plotted against R in Fig. 7, for the two runs. The dashed line refers to the particle density, $n_{\rm part}$, normalized to the halo density in the interval $[R_{200}, R_{\rm ta}]$. (In this plot we use all haloes with $v_{\rm peak} > 80\,{\rm km\,s^{-1}}$; here, as well as in the other analyses, we have examined the effect of changing this threshold and found that, within our statistical uncertainties, there are no significant variations.)

Beyond the virial radius of the clsuter the curves for haloes and particles have similar slopes. Within the virial radius of the cluster we see that the halo distribution is 'antibiased', i.e. less concentrated with respect to the mass distribution. The halo number density profile is consistent, for $R > 1\,{\rm Mpc}$, with the average galaxy number density profile derived by Carlberg et al. (1997b) for the clusters of the CNOC survey. However, the average cluster mass profile that they derive from the same data is much shallower than that of the relatively small cluster analysed here.

If the scaled particle distribution is regarded as the 'asymptotic' halo distribution, in the case of no bias and infinite resolution (and sufficiently small physical cores), then integrating the difference between the curves over R would give an estimate of the number of missing haloes. With this assumption, we find for RUN2 that ∼240 haloes are 'missing', about 50 per cent of the haloes with $v_{\rm peak} > 80\,{\rm km\,s^{-1}}$. The systematic difference between RUN1 and RUN2 makes tidal disruption of 'softened' haloes the most likely cause of this halo antibias. This may be overcome with higher resolution simulations that accurately resolve the structure of the smallest haloes. However, the destruction of haloes may not be caused by numerical resolution alone. For example, binary mergers between haloes of similar mass will lead to a single halo with no memory of its history. These mergers may be important in the early phases of the formation of a cluster.

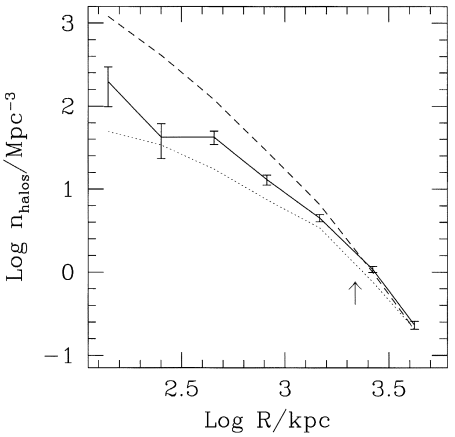

Figure 7. The number density of haloes with $v_{\rm peak} \geq 80\,{\rm km\,s^{-1}}$ as a function of R, for RUN1 (dotted line) and RUN2 (solid line); the former has a spline softening length of 10 kpc, twice that of the latter. The dashed line is the particle density scaled in such a way that, in the distance interval $[R_{200}, R_{\rm ta}]$, the *scaled* number of particles equals the number of haloes. The error bars are 1σ Poissonian errors from the counts in each bin; the arrow marks the value of R_{200}.

4.3 Distribution of halo radii

The extent of dark matter haloes attached to galaxies in clusters has become directly observable via observations of gravitational lensing (Geiger & Schneider 1998; Natarajan et al. 1998). Here we can make some predictions for future surveys that will constrain the extent of haloes as a function of position from the cluster centre.

The projected distribution of the haloes within the boundaries of the cluster was shown in the lower panel of Fig. 1. There is a clear decrease of halo sizes near the cluster centre even in this projected plot (there is little difference if we include haloes up to twice R_{200}).

Fig. 8 shows the average value of $r_{\rm halo}/R_{200}$ as a function of clustercentric position, R/R_{200}, at redshifts $z = 0$ and $z = 0.5$. We use R_{200} at each z as the length unit to highlight the self-similarity in the evolution of the cluster substructure. Halo radii clearly decrease as we move towards the cluster centre, but the trend is hard to detect at $z = 0.5$ because the cluster has accreted only relatively few haloes (of $v_{\rm peak} > 80\,{\rm km\,s^{-1}}$), has a quite anisotropic mass distribution and tides have been efficient only in its very centre. The mean size of haloes beyond R_{200} is ≳8 per cent of R_{200} and drops approximately linearly to zero as we move from the virial radius to the cluster centre. (In Fig. 8, halo radii are those measured from the circular velocity profiles; the results using SKID radii are very similar.) As shown in the lower panel of this figure, projection effects weaken but do not erase the trend of halo radii with R (here we have included haloes up to $1.5R_{200}$, but it makes little difference changing the limiting R between 1 and 2 times R_{200}). Natarajan et al. (1998) do not detect a dependence on R, but presently the observational uncertainties are large and the radial range of the data is limited.

Halos of different $v_{\rm peak}$ obviously have intrinsically different sizes. We can interpret Fig. 8 and account for this intrinsic scatter using our 'locally stripped isothermal onion approximation' (with $v_{\rm c} \equiv v_{\rm peak}$; see Section 4.1) and considering the ratios $\eta \equiv r_{\rm halo}/(h^{-1}v_{\rm peak})$. When haloes form in isolation, $r_{\rm halo} \equiv r_{200} \approx h^{-1}v_{\rm c}$ and $\eta \simeq {\rm const} \simeq 1\,{\rm kpc/\,km\,s^{-1}}$. Within the cluster, $r_{\rm halo} \equiv r_{\rm tid} \simeq Rv_{\rm c}/V_{\rm c} \simeq (h^{-1}v_{\rm c})R/R_{200}$ and $\eta(R) \simeq R/R_{200}$. If haloes have gone past pericentre $r_{\rm peri}$ and their radii $r_{\rm tid}$ are determined by $\bar{\rho}_{\rm C}(r_{\rm peri})$, then η will be smaller by a factor of $r_{\rm peri}/R$.

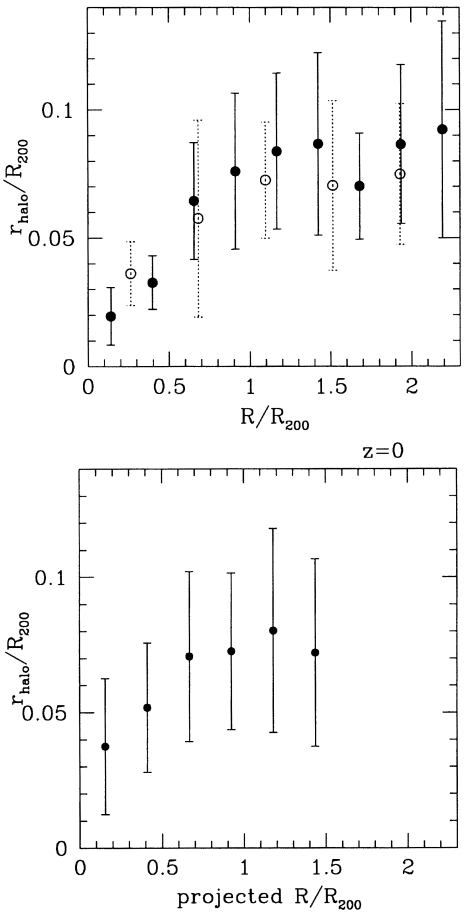

Figure 8. In the upper panel, the average value of halo radii is plotted against clustercentric position at redshift $z = 0$ (solid symbols) and $z = 0.5$ (dotted symbols), for haloes with $v_{peak} \geq 80\,km\,s^{-1}$. The lower panel shows the distribution against projected distance at $z = 0$. At each z, the unit is the virial radius of the cluster at that epoch. The error bars give the dispersion about the average. Note that the most massive cluster halo at $z = 0$ has been excluded from the average; it has a radius of 470 kpc and is located at $R = 0.9R_{200}$.

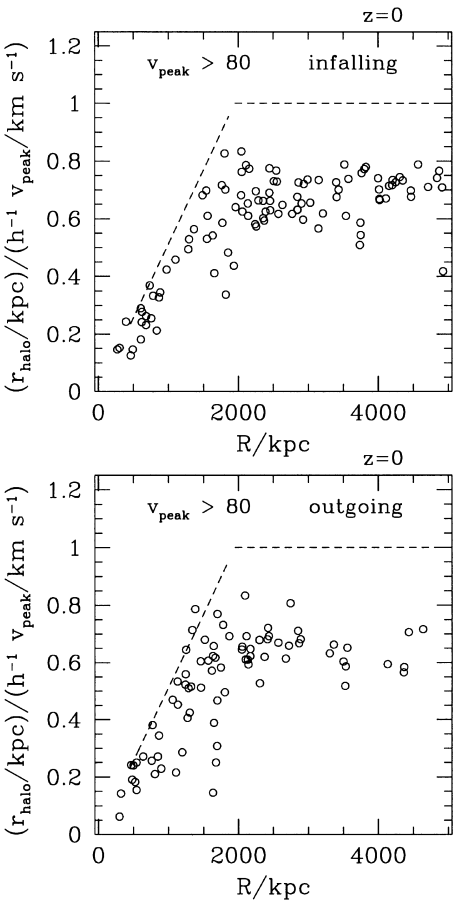

Figure 9. The figure highlights the effects of tidal stripping on halo sizes at varying distance from the cluster centre (haloes with $v_{peak} > 80\,km\,s^{-1}$). For peripheral haloes the ratio $r_{halo}h/v_{peak}$, with $h = h_0(1+z)^{1.5}$ and units of kpc and $km\,s^{-1}$, is approximately 70 per cent of the value expected for a purely isothermal mass distribution (in agreement with their profiles being of NFW type; see Section 5.1). The dashed line gives the expected behaviour for isothermal haloes being instantaneously stripped whilst falling into the deeper potential of the cluster. The upper and lower panels are for inward and outward-moving haloes respectively. See the text for further details.

In a fully virialized system there is no difference between the motions away and towards the centre of the system. However, in a $\Omega = 1$ cosmology clusters never stop accreting material and we might expect some different morphologies between ingoing and outgoing haloes. Moreover, haloes reaching apocentres beyond the boundaries of the cluster might be heated by low-speed encounters with other haloes and re-expand, partly covering the effects of tides at the previous passage at pericentre.

The distribution of η at $z = 0$ is shown in Fig. 9. It has a trend similar to that expected for locally truncated isothermal spheres (dashed line). The separation between the latter and the points in the 'periphery' ($R > 2$ Mpc) is a measure of the departure of the actual density profiles of peripheral haloes from isothermal. All outgoing haloes must have necessarily passed their pericentres; therefore η should depart from the dashed line more than for infalling haloes, and we do observe evidence of this effect in the figure. The corresponding results using SKID halo radii are shown in Fig. 10 which also shows results for $z = 0.5$ [only for haloes with $R < R_{200}$; note the different scale on the horizontal axis from $z = 0$ to $z = 0.5$; $h = h_0(1+z)^{1.5}$ is H_z in units of 100 Mpc/ $km\,s^{-1}$]. The results for $z = 0$ confirm the general picture illustrated by the previous Fig. 9, but here the points have a larger scatter and the trend with R is weaker, especially for outgoing haloes: this is expected because, in the 'dynamical' definition used by SKID, the tidal radii are less sensitive to $\rho_{bkg}(R)$. At $z = 0.5$, there is evidence that tidal effects are already operating at this relatively high redshift, in agreement with the trend shown by Fig. 8.

4.4 Fraction of mass in haloes

Fig. 11 shows the fraction of the mass attached to haloes. As expected, it decreases sharply approaching the cluster centre: it is $\lesssim$5 per cent at $R \lesssim 500$ kpc and increases to $\sim$20 per cent at R_{200}. The total fraction of mass attached to haloes within R_{200} is about 13 per cent. (These values do not depend sensitively on the adopted value of the softening parameter.) Outside the cluster, the haloes account for about 20 per cent of the total mass. The peak at $R\sim$ 1.5 Mpc is not significant: it is caused by the largest halo within the cluster of mass $2.3 \times 10^{13}\ M_\odot$ that contributes alone 5 per cent of the total mass of the cluster and half of the mass in that bin.

We can compare the mass fraction of peripheral haloes with the Press–Schechter approximation (Press & Schechter 1974), using

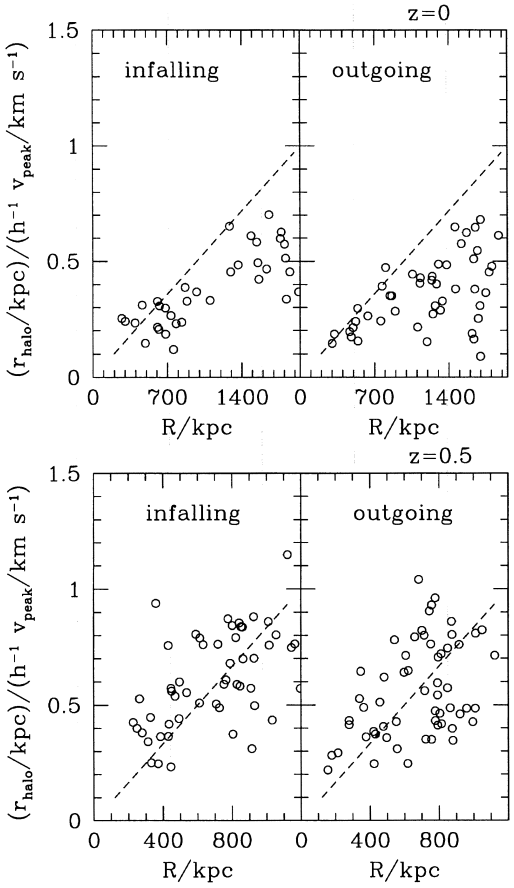

Figure 10. Same as in Fig. 9 but the halo radii are measured using the SKID algorithm, which discards unbound particles, and data are shown for $z = 0.5$ too (lower panels). Only data for cluster haloes are plotted; at $z = 0.5$, the formal virial radius of the cluster is $R_{200} = 1200$ kpc.

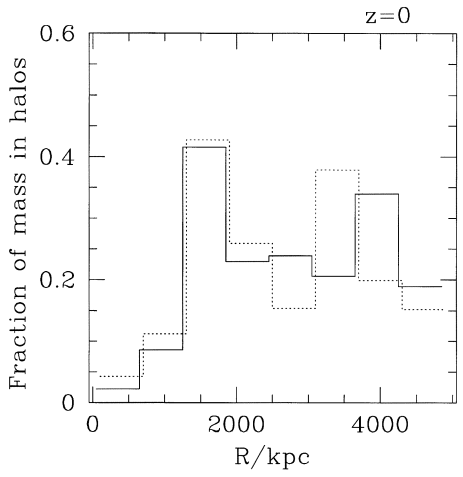

Figure 11. Fraction of mass within resolved haloes in spherical shells of thickness 600 kpc versus cluster-centric position at $z = 0$. The solid line is for RUN1 and the dotted line is for RUN2 (slightly shifted for clarity).

again a routine supplied by P. Tozzi. Adopting a minimum halo mass of 1.35×10^{10} $M_\odot$ (16 particles) and the mass of the most massive peripheral halo (3.4×10^{12} $M_\odot$), we find ~0.25 from the analytical theory, in good agreement with the average of the last five outer bins, ~0.23.

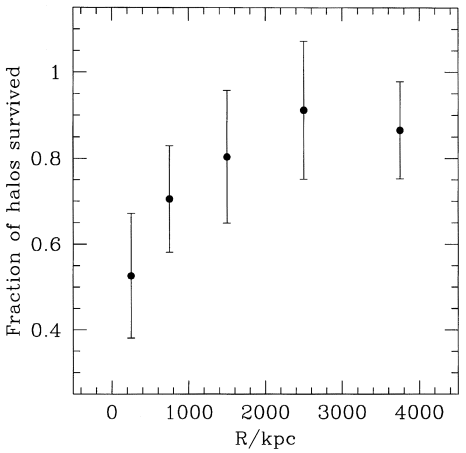

Figure 12. Fractions of $z = 0.5$ haloes above resolution that have a descendent halo identifiable at $z = 0$; the error bars are 1σ Poissonian uncertainties estimated from the numbers of haloes in each distance interval (the plot also gives roughly the probability that a $z = 0.5$ halo survives to $z = 0$ keeping more than ~50 per cent of its original mass; see text for details).

4.5 Merging and 'surviving' haloes

Comparing the distribution of the haloes at $z = 0.5$ and $z = 0$, we can determine the merger rate and the fraction of haloes that can be traced to the present epoch. We selected all the haloes with more than 32 particles at $z = 0.5$ and examined their association with haloes with more than 16 particles at $z = 0$. We determine that a high-z halo is the progenitor of a low-z halo if the latter contains at least a significant fraction of the mass of the former, say 25 per cent. However, to account for mass loss via tidal stripping we need be less restrictive; therefore we considered also an extreme mass fraction cut-off of 1 per cent, but our results are not very sensitive to this limit. (The results for RUN2 and RUN1 are similar, in agreement with the fact that the loss of substructure because of poor resolution occurs largely during the assembling of the mass of the cluster).

We find, for haloes with apocentres $r_{apo} \geq R_{200}$ and at least one progenitor among those identified at $z = 0.5$, that 5–9 per cent of them, depending on the mass fraction cut-off, are the product of a merger. There are a large number of mergers among haloes with apocentres close to R_{200} (3–5 out of 17). However, of the 38 haloes with $r_{apo} \lesssim 80$ per cent R_{200}, none has merged. We find no evidence for merging once the haloes have entered the cluster. This seems to argue against the possibility of Butcher–Oemler (1978, 1984) galaxies being cluster members with star formation switched on by mergers in the cluster environment (Couch et al. 1994).

Fig. 12 shows the fraction of haloes identified at $z = 0.5$ in different distance intervals that are also associated with $z = 0$ haloes (for RUN1). Although we adopt the extreme 1 per cent mass fraction cut-off to establish this association, the results shown in the figure essentially give the probability that haloes will survive with ~50 per cent of their original masses attached. In fact, $z = 0.5$ haloes with masses close to the limit of 32 particles will be resolved at the 16-particle limit of the $z = 0$ sample only if they have not lost more than ~50 per cent of their masses, and small haloes dominate the statistics (note that, for our choices of the mass and force resolutions, even haloes with a few tens of particles should be stable over the interval considered here, according to the analysis of Moore et al. 1996). At $R \lesssim 0.5$ Mpc, such probability is ~0.5,

against a value of order unity in the cluster periphery. This result is confirmed if we repeat the analysis for larger haloes; however, the statistical uncertainties are quite large and we plan to study this issue in more detail using new high-resolution simulations.

4.6 Orbital parameters

We now shift our attention to the motions of the haloes within the cluster. Halos that follow radial orbits are more likely to be disrupted than haloes that have circular motions, since the former penetrate further into the cluster potential well. Do we detect a bias in favour of circular orbits? We calculate orbits by approximating the cluster potential as a spherical static potential, computed using the density profile at $z = 0$ and then using the position and velocity information for the haloes. For comparison, we also compute the orbits of a random subset of 20 000 particles.

In the upper panel of Fig. 13 we plot the ratios $r_{\rm peri}/r_{\rm apo}$ versus R for the haloes of RUN2 (RUN1 gives identical results). The lower panel shows the average values of this ratio for the haloes (solid line) and the particle sample (dotted line). We find that radial orbits are quite common and circular orbits are rare. The median ratio of apocentre:pericentre is approximately 6:1 and nearly 25 per cent of the haloes are on orbits more radial than 10:1. A rough calculation by the authors reveals that this is very close to an isotropic orbital distribution within an infinite isothermal potential. (In this calculation we assumed random velocities of particles that orbit within an equilibrium $1/R^2$ density distribution.)

We do not detect a large difference between halo orbits as a function of R, nor do we find a difference between the orbits of the particle background and the haloes. This is surprising since we expected to find fewer haloes on radial orbits near the cluster centre. The expected bias could be disguised if the central overmerging problem originated within the dense clumps that formed before the final cluster. Finally, we note that the radial velocity dispersion of the haloes within the cluster is 720 km s^{-1}, a value that is within a few per cent of the dispersion of the background particles – even when only the most massive haloes are considered.

Information on the distribution of the orbital parameters of haloes can be used to model the effects of tidal stripping and dynamical friction for haloes within haloes in semi-analytic models of structure formation based on the Press–Schechter approximation. Figs 14 and 15 plot the probability density distributions of 'circularities' and pericentres for cluster (solid line) and peripheral (dashed line) haloes. For each halo, the 'circularity' $\epsilon \equiv J/J_{\rm C}(E)$ is defined as the ratio of its angular momentum to that of a circular orbit with the same energy (Lacey & Cole 1993). There are no marked differences between the two groups of haloes, although the orbits of cluster haloes are more close to circular and penetrate further into the cluster than those of peripheral haloes. Among the latters, 15 per

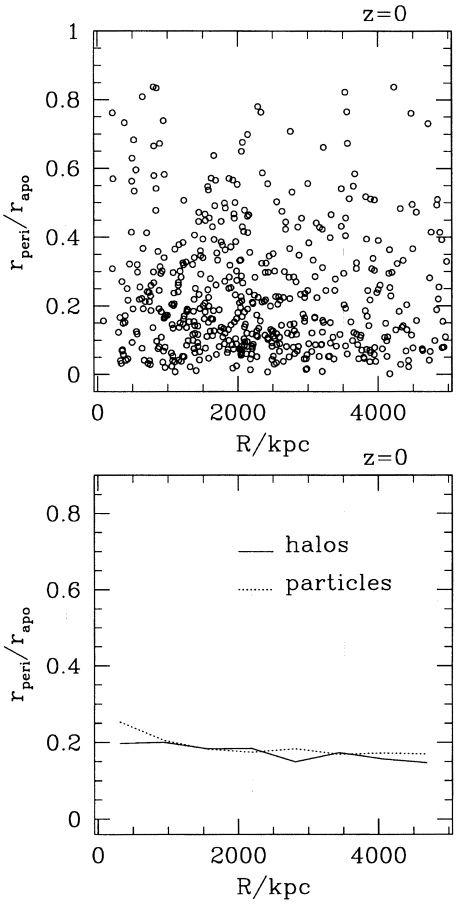

Figure 13. The upper panel shows the ratio of pericentric and apocentric distances for each halo plotted against its current position. The lower panel shows the average value of these ratios for the haloes (dashed curve) and a random subsample of cluster dark matter particles (solid curve).

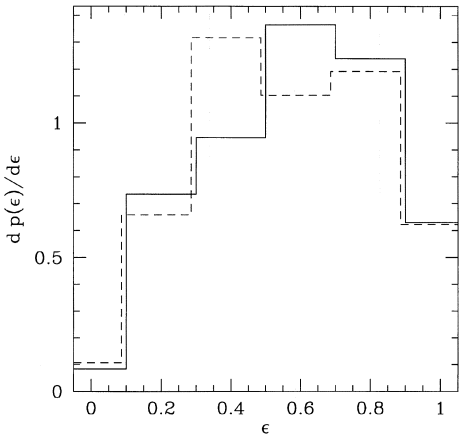

Figure 14. Probability density distribution of halo 'circularities' $\epsilon \equiv J/J_{\rm C}(E)$ (see text) for *cluster* ($R < R_{200}$; solid line) and *peripheral* haloes (dashed line).

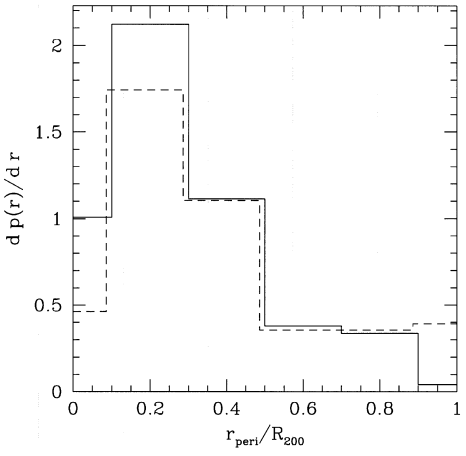

Figure 15. Probability density distribution of halo pericentres $r_{\rm peri}$ (line styles as in Fig. 14).

cent have pericentres outside the boundaries of the cluster and 9 per cent come as close as 200 kpc ($0.1R_{200}$) to the centre of the cluster. This condition is twice as frequent among cluster haloes; in the whole sample the fraction of $r_{\rm peri} < 200$ kpc is 14 per cent. These results are in good agreement with results presented by Tormen (1997).

For such radial orbits, we expect that the tidal radii of the haloes are determined primarily by the global tidal field of the cluster. We can check if this is correct by estimating the truncation radius at the pericentre of each halo using $r_{\rm tid} \simeq r_{\rm peri} \times v_{\rm peak}/V_{\rm c}$ [the use of $V_{\rm c}(R)$ at $R = r_{\rm peri}$, instead of the constant value $V_{\rm c} = V_{200} = 1000\,{\rm km\,s^{-1}}$ does not make any detectable difference, because the variation of $V_{\rm c}(R)$ is $\lesssim$10 per cent in the range $0.05 < R/R_{200} < 1$]. We can test this prediction for our outgoing haloes that must have passed pericentre recently, enhancing the likely validity of our approximation. In Fig. 16 we plot the expected tidal radius, according to the above formula, against the value measured, for both methods [from SKID and from the circular velocity profile $v_{\rm c}(r)$]. The agreement is excellent for the SKID values, with the exception of the points marked as stars. These latter points represent haloes that are on very eccentric orbits such that $r_{\rm peri}$ is less than 300 kpc. These haloes are more likely to suffer impulsive collisions with other haloes as they pass close to the cluster centre. We note that many of these haloes have tidal tails that may cause the measured tidal radii to be overestimated. The scatter in the correlation increases when we measure halo sizes using the halo circular velocity profiles, but the trend is still apparent. The radii estimated with this method are more sensitive to tidal tails than SKID radii, since the latter can discard the unbound streams of particles. This is the reason why some points in the lower panel of the figure correspond to larger $r_{\rm tid}$ than those in the upper one.

Recalling Figs 9 and 10, we can now check if tidal stripping is indeed responsible for the low values of $\eta \equiv r_{\rm halo}/(h^{-1}v_{\rm peak})$. Using the information on $r_{\rm peri}$, we can 'correct' the values of η for outgoing haloes as $\eta \rightarrow \eta \times R/r_{\rm peri}$. The effect of this correction is shown in Fig. 17, in which the open circles are the original points of the upper right panel of Fig. 10 and the filled circles are 'corrected' As expected, the 'corrected' η scale as R/R_{200}. In conclusion, the isothermal model predictions for the tidal radii work well when the pericentric positions of the haloes are used. In turn, this good agreement confirms that the estimates of the orbital parameters for cluster haloes in the spherical static potential approximation are a good description of their actual motions.

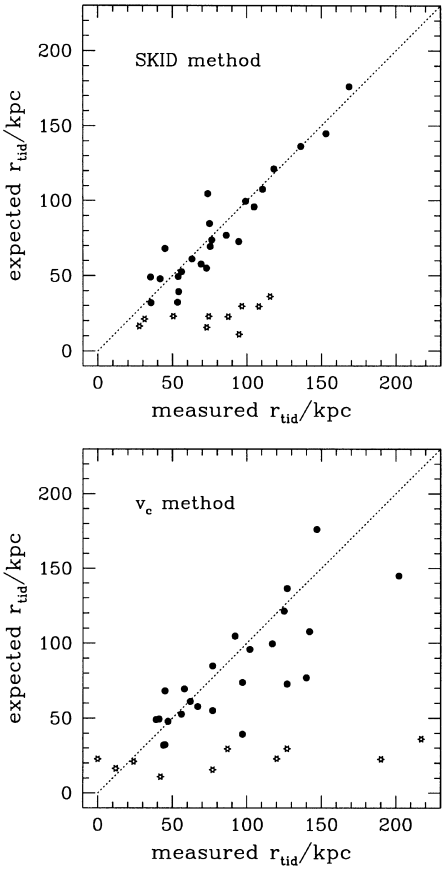

Figure 16. We plot the measured values of halo tidal radii against their expected values, assuming that the haloes have isothermal mass distributions that are tidally stripped at their pericentric positions. The upper panel uses halo tidal radii measured using SKID, therefore only self-bound particles are included to determine halo sizes; the '$v_{\rm c}$' method uses halo circular velocity profiles and includes the cluster background. The points represent outgoing haloes (at $z = 0$) with $R \leq 0.8R_{200}$; the stars denote those with $r_{\rm peri} < 300$ kpc.

5 HALO INTERNAL PROPERTIES

We shall now examine the internal structure of haloes in more detail with the main objective of studying how the cluster environment affects them. In particular, we shall focus on the distribution of $r_{\rm peak}$ and $v_{\rm peak}$, which provide information on their internal concentrations. Then we shall study in detail a small subsample of well-resolved haloes and examine their density profiles and the compatibility with the analytic fits generally adopted in the literature to describe dark matter haloes (Hernquist 1990; Navarro et al. 1996).

5.1 Statistical distribution of halo properties

A detailed analysis of isolated cold dark matter haloes in N-body simulations has been carried out by Navarro et al. (1996) and Navarro, Frenk & White (1997); NFW in the following. Their simulations had a mass resolution such that individual haloes

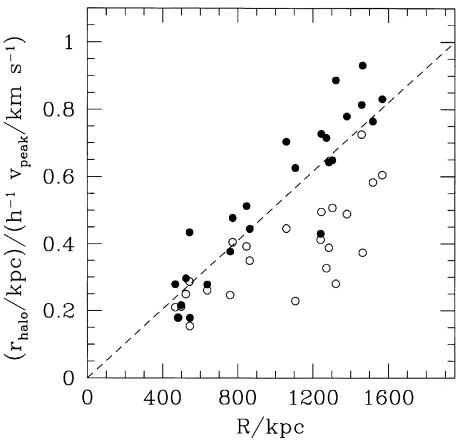

Figure 17. The dashed line gives the expected dependence on R of the ratios $\eta \equiv r_{\rm halo}/v_{\rm peak}$ for isothermal haloes that are tidally limited by the cluster at a distance R as they fall into the cluster for the first time. Such ratios attain a minimum when haloes reach pericentre and are maximally stripped; therefore, moving away from the centre of the cluster, outgoing haloes have values of η systematically below the line (the open circles; same as in the upper-left panel of Fig. 10). If we 'correct' their ηs using the information on their pericentres, the points are brought back to the line (the filled circles).

contained of the order of 10 000 particles and force softening that was 1 per cent of the final virial radii. Over a wide range of masses, NFW found relations between the properties of their profiles, $r_{\rm peak}$ and $v_{\rm peak}$, and their virial masses M_v. Furthermore, the density profiles of haloes could be fitted by a universal formula with varying concentrations, c, that can be predicted from their masses within a given cosmological model.

Here we want to address two questions.

(i) Do the same relations found by NFW for isolated haloes hold for the *peripheral haloes* that surround the virialized cluster? These are relatively isolated, but they evolved in an environment that is special owing to the nearby cluster. For instance, the streaming motions it induces could have determined peculiar merging histories of the peripheral haloes, and merging may play a crucial role in shaping their internal structures (cf. Syer & White 1997; Moore et al. 1998).

(ii) Do the same relations apply for *cluster haloes*, which are affected by tidal stripping and halo–halo encounters? Cluster haloes could also have peculiar properties reflecting the high-density environment in which they formed.

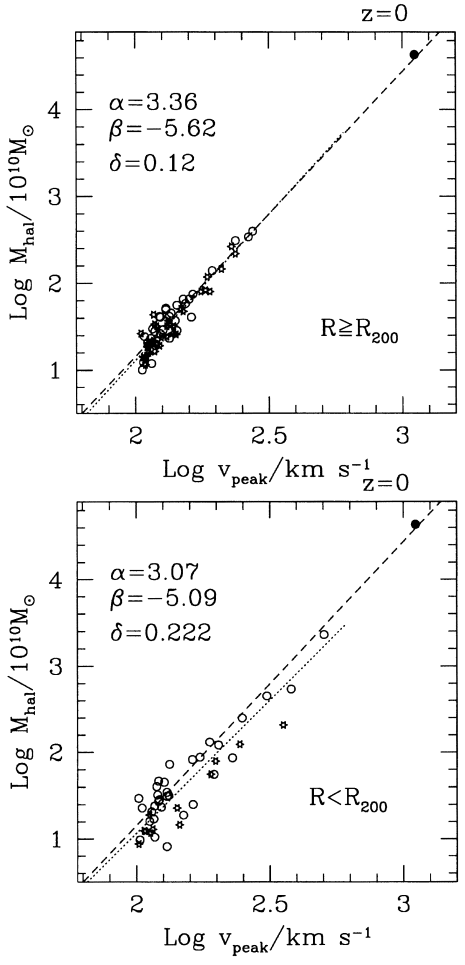

Figure 18. Distribution of halo masses versus $v_{\rm peak}$ for 'peripheral' (upper panel) and cluster haloes (lower panel) at $z = 0$. The stars mark inner points, with $R < 1.5R_{200}$ and $R < 0.6R_{200}$, respectively for the two groups. The filled circle gives the values for the entire cluster. The dashed line is the power-law fit obtained by Navarro et al. (1996) for isolated haloes. The dotted lines are similar power-law fits to the data of the form $M = 10^{\beta} v^{\alpha}$, and δ is the rms scatter in mass about the fit.

These two factors could then affect the properties of our halo sample in such a way that, for instance, the ratios $v_{\rm pk}/r_{\rm pk}$, which reflect the concentrations of the haloes, are systematically higher than for the field population (e.g. cluster haloes form earlier or are biased towards high concentrations such that they have survived tidal disruption) Alternatively, impulsive mass loss may cause haloes to subsequently 'relax' and re-expand towards an 'equilibrium' configuration. This could be detected as a change in concentration versus orbital position.

We shall focus on the following two relations, for cluster and peripheral haloes, $M_{\rm halo}$ versus $v_{\rm peak}$ and $r_{\rm peak}$ versus $v_{\rm peak}$. The former is interesting because it relates masses to velocities, which are in principle more easily observable, whilst the latter gives information on halo concentrations and the related issues discussed above. ($M_{\rm halo}$ is the halo mass defined by the inflexion point of the circular velocity profile, after subtracting the contribution from the smooth particle background, as explained in Section 3.3).

The distribution of halo masses versus $v_{\rm peak}$ is illustrated in Fig. 18, for peripheral (upper panel) and cluster (lower panel) haloes and compared with the relation found by NFW within the cosmological model we have adopted (NFW 1996; dashed line). (For clarity, only points with $v_{\rm peak} > 100\,{\rm km\,s^{-1}}$ are shown, since the noise is large for small haloes.) In each panel, the stars mark *inner* haloes of each group (see the caption of the figure for details; note that some inner haloes within the present 'periphery' sample

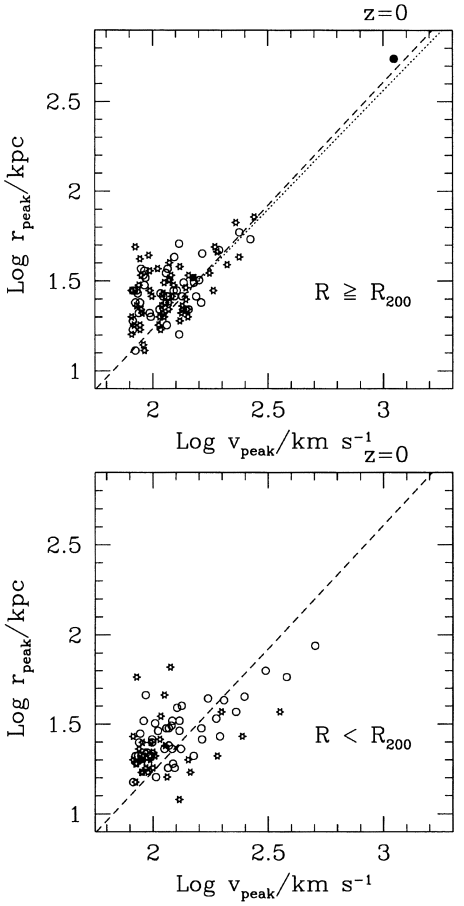

Figure 19. Distribution of $v_{\rm peak}$ and $r_{\rm peak}$ for peripheral (upper panel) and cluster haloes (lower panel) at $z = 0$. The points have the same meanings as in Fig. 18. As before, the dashed line gives the expected relation for isolated haloes (Navarro et al. 1996) and the dotted line is a fit to the points with $v_{\rm peak} \geq 150\,{\rm km\,s^{-1}}$.

have highly radial orbits and were inside the cluster at an earlier epoch). For peripheral haloes, the agreement between our data and the NFW curve is excellent (note that most of the scatter results from points with $v_{\rm peak} < 150\,{\rm km\,s^{-1}}$ that may be affected by the numerical noise). Cluster haloes have a much larger scatter and the fit is shallower. Their masses are smaller for a given $v_{\rm peak}$, as naturally expected for stripped haloes, and this is most noticeable for the *inner* cluster haloes.

The distribution of $v_{\rm peak}$ and $r_{\rm peak}$ is shown in Fig. 19, again for peripheral haloes in the upper panel and cluster haloes in the lower panel. The dashed line gives the relation for the haloes studied by NFW and the dotted line in the upper panel is a power-law fit to the haloes with $v_{\rm peak} > 150\,{\rm km\,s^{-1}}$ (which appear to be less affected by noise). The behaviour of the peripheral haloes clearly agrees well, within the scatter, with that expected from the analysis of NFW. On the contrary, cluster haloes lie significantly below the dashed line: they are skewed towards smaller values of $r_{\rm peak}$ for a given $v_{\rm peak}$, with a more prominent effect for the innermost haloes.

At $z = 0.5$, we observe a behaviour similar to that at $z = 0$, as is shown in Figs 20 and 21 (in these figures, the dotted line is again a fit to the points with $v_{\rm peak} > 150\,{\rm km\,s^{-1}}$ and the dashed line, the relation of the NFW at $z = 0$, is drawn for comparison).

In conclusion, the high-density regions of the cluster and the 'accelerated collapse' of the cluster haloes can affect not only the sizes of the haloes but also their internal structures. We examine this issue further in the next section by looking in detail at the properties of a sample of large well-resolved haloes.

5.2 The large halo sample

We now restrict our analysis to several well-resolved, massive haloes that are not as affected by force softening or mass resolution, by following the evolution of those haloes that have $r_{\rm peak} > 25\,{\rm kpc}$ and $v_{\rm peak} > 150\,{\rm km\,s^{-1}}$ [from Fig. 19 we can see that these values delimit a region in the plane $(v_{\rm peak}, r_{\rm peak})$ where the properties of haloes behave quite regularly].

To highlight differences between 'cluster haloes' and 'peripheral haloes', we selected two groups in the distance ranges $R/R_{200} \leq 2/3$ and $4/3 < R/R_{200} < 7/3$. Again, these values of R correspond to those roughly separating different halo behaviours in Fig. 19. These selection criteria yield seven haloes in the first distance range (although names like 'Yogi', etc... would be preferable, for brevity's sake we shall simply call them A, B, C, D, E, F) and seven in the second one (G, H, I, L, M, N, O). The first 3 of each group lie in the inner part of their distance ranges ($R \lesssim 0.8$ Mpc and 2.8 Mpc $\lesssim R \lesssim 3.5$ Mpc, respectively). All of these haloes contain at least 1000 particles within $r_{\rm halo}$. We excluded halo 'O' because it is the product of a recent merger ($z \sim 0.5$). All of the other haloes have only one progenitor at $z = 0.5$ and the inner haloes are well defined up to $z \sim 2$.

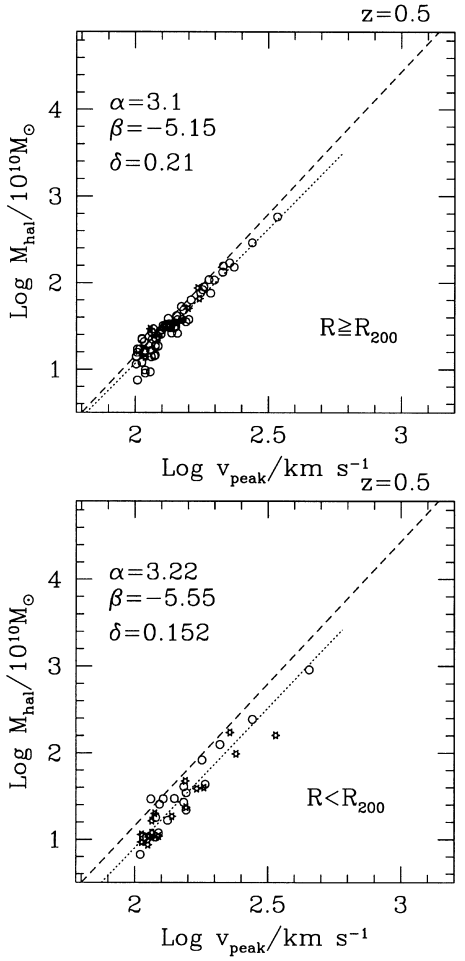

Figure 20. Symbols and lines are the same as in Fig. 18 but for $z = 0.5$. Here, R_{200} is the formal virial radius of the cluster at that epoch.

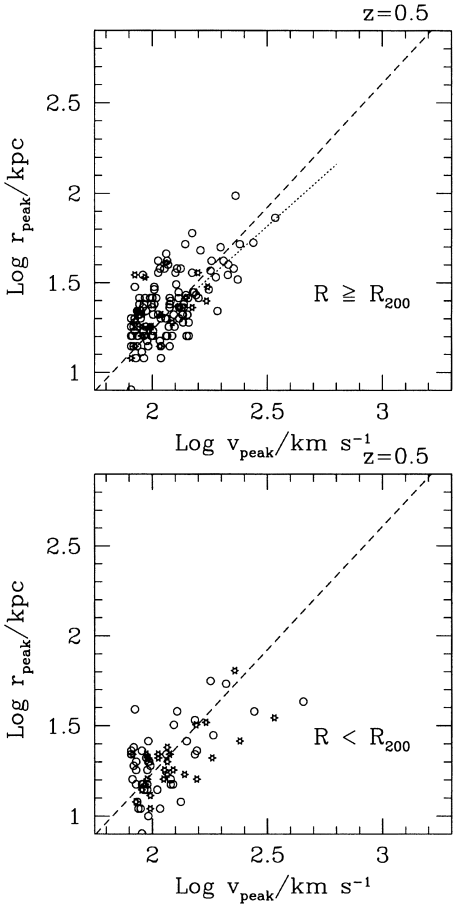

Figure 21. Symbols and lines are the same as in Fig. 19 but for $z = 0.5$. Here $R_{200} = 1.2$ Mpc is the formal virial radius of the cluster at that epoch.

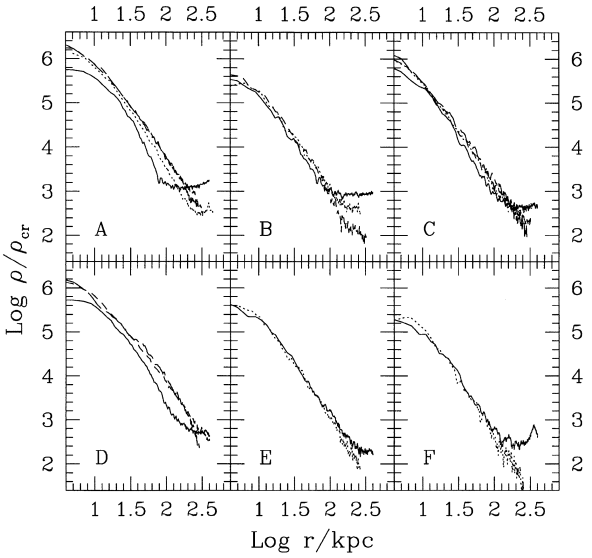

Figure 22. Evolution of the density profiles of a sample of massive cluster haloes after their last major mergers. The solid, dotted, short-dashed and long-dashed lines are the profiles measured at $z = 0, 0.5, 1$ and 1.8 respectively (some haloes have their last major mergers at $z \geq 1$ and correspondingly not all lines are shown; the $z = 0.5$ profile of D could not be measured because this halo was too close to the cluster centre at that epoch). The radius r is the distance from the halo centres in physical kpc and ρ is measured in units of today's critical density $\rho_{0,\mathrm{cr}}$.

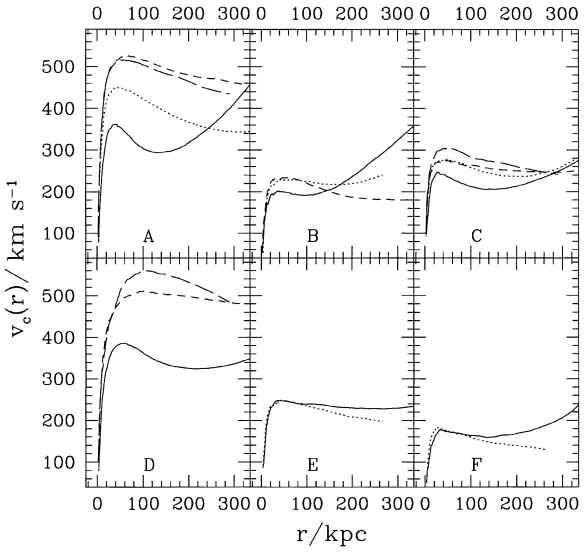

Figure 23. Evolution of the circular velocity profiles for the same haloes as in Fig. 22, plotted using the same line types at the different redshifts. The velocities are measured in physical $\mathrm{km\,s^{-1}}$.

5.2.1 *Evolution of the profiles*

We now examine the evolution of the density profiles for this sample of haloes. We consider four values of the redshift: $z = 0, 0.5$, 1, and 1.8. In our sample, all peripheral and *outer* cluster haloes show evidence of major mergers at $z \sim 1$, but the inner cluster haloes (A to D) have a well-defined major progenitor up to $z = 1.8$ (although they have captured many small satellites and experienced minor mergers since $z \sim 1$). For peripheral and outer cluster haloes we limit our analysis to $z = 0.5$, while for the innermost ones we will examine the profile data up to $z = 1.8$.

Fig. 22 shows the evolution of $\rho(r)$ for the cluster haloes. All the curves for the present epoch flatten at large r where the smooth particle background density of the cluster, ρ_{bkg}, starts dominating (haloes from left to right in each row of figures have increasing distances from the cluster centre). Such flattening also appears in the profiles of the $z = 0.5$ progenitors of A, B and C because they are within the high-density environment of the forming cluster at that epoch.

The features of $\rho(r)$ are highlighted in the corresponding circular velocity profiles $v_{\mathrm{c}}(r)$ shown in Fig. 23. Note that the location and height of the peak of $v_{\mathrm{c}}(r)$ have both changed for the *inner* haloes (upper panels), whilst the profiles of the *outer* haloes E and F, in the lower panels, are remarkably stable, apart from the change in ρ_{bkg}.

Halos A and D show the most significant evolution and have quite steep outer slopes. Halo A formed at the intersection of the two filaments the collapse of which originated the cluster, and its structure has been heavily disrupted by the tidal field there, causing it to lose a huge amount of mass. Halo D formed in the outer part of one of the filaments, and its fate has been similar. Halos B and C have also evolved, but the changes have not been so dramatic. The values of v_{peak} have decreased however by $\sim$15 per cent between $z = 0.5$ and $z = 0$. The remaining haloes E and F, which do not show signs of significant evolution, formed in the periphery, but at $z = 0$ they are moving outwards. However the pericentre of F is close to its present distance ($\sim$1.3 Mpc). That for E is $\sim$600 kpc, yielding an expected tidal radius of $\sim$150 kpc; this agrees very well with the SKID value, but is 25 per cent smaller than the tidal radius measured from the density profile [directly from $\rho(r)$, or from $v_{\mathrm{c}}(r)$]. This is due to the anisotropic distribution of mass around E, which appears stretched along the orbit with a 'trail' of particles on both sides. This tidal debris was contained within its virial radius at $z = 0.5$ and, though stripped during the passage at pericentre and presently unbound to it, is still moving closely, apparently on the same orbit. The lack of evolution in the density profile of E is then due to the assumption of spherical symmetry and the contribution from unbound particles nearby.

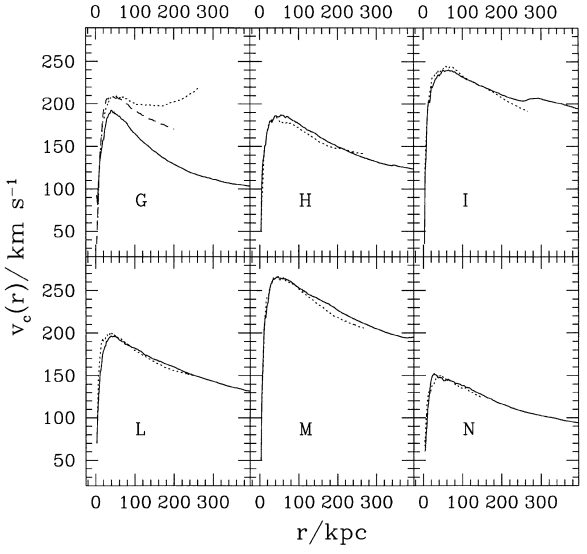

Figure 24. Evolution of the circular velocity profiles of a sample of peripheral haloes after their last major mergers. The dotted and short-dashed lines correspond to the redshifts $z = 0, 0.5, 1$. (At $z = 0$, halo G has a distance from the cluster centre $\sim 4/3 R_{200}$ but was inside the cluster at earlier epochs.

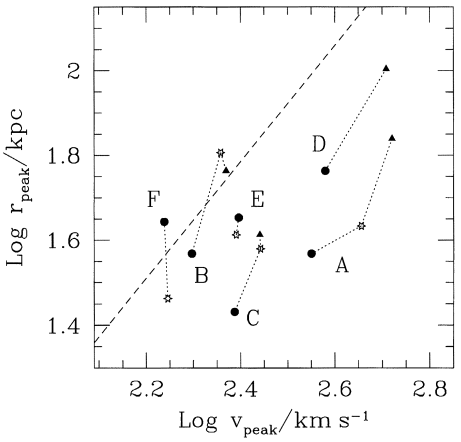

Figure 25. Evolution of the cluster haloes of Fig. 22 in the plane ($v_{\rm peak}, r_{\rm peak}$). The positions at $z = 0$ are plotted as filled circles, those at $z = 0.5$ as stars (not for D) and at $z = 1$ as triangles (only for A–D). The dashed line is the relation expected for isolated haloes at $z = 0$ from Navarro et al. (1996) as in Fig. 19.

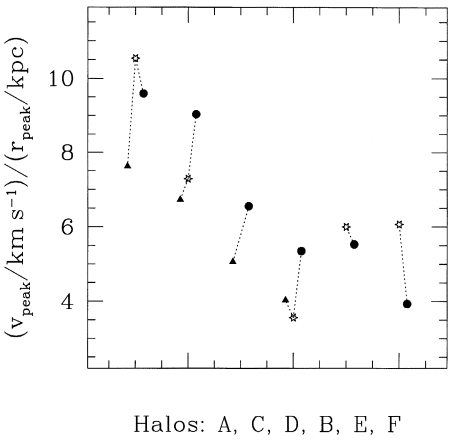

Figure 26. Evolution of 'concentrations' $v_{\rm peak}/r_{\rm peak}$ for the haloes of Fig. 25; the points represent the same redshifts as before. The haloes are ordered from left to right according to the overdensity of the region where they formed: A and B formed at the intersection of the filaments the collapse of which originated the cluster, D along one of the filaments and the others in the 'field'.

Finally, Fig. 24 shows the corresponding $v_{\rm c}$ profiles for the six peripheral haloes considered. Except for case G, these haloes have never entered the cluster and their profiles show no significant differences between $z = 0$ and 0.5. Halo G formed in the periphery but has been orbiting through the cluster since $z \sim 0.5$ and has clearly lost mass.

In summary, of the large cluster haloes identified at $z = 0$, only those with $R \lesssim R_{200}/2$ have density profiles significantly different from those they had before the formation of the cluster. However, one of the large haloes in the outskirts of the cluster has survived a passage (or more) at pericentre and has evolved considerably too. In particular, the values of $v_{\rm peak}$ can change: $\sim$10 per cent in three cases, but 20–25 per cent in two other cases.

It is interesting to examine how the haloes 'move' in the plane ($r_{\rm peak}$, $v_{\rm peak}$) of Fig. 19, in order to determine if their evolution (under tidal stripping or halo–halo encounters) is the reason for the systematically lower $r_{\rm pk}$ for the cluster haloes with respect to field haloes of the same $v_{\rm pk}$. Fig. 25 shows the evolution of $r_{\rm pk}$ versus $v_{\rm pk}$ for the six cluster haloes considered previously from $z = 1$ (when available) through 0.5 to $z = 0$ (from triangles to stars to circles in the figure). From these data, it seems that the points did not move significantly *away* from the curve of the NFW. They move *parallel* to the line rather than downwards and those farthest from the line are also those that formed the nearest to primordial high-density regions (A and C, which formed near the centre of the cluster, but also D, which formed in one of the giant filaments that merged into it). This could be evidence that haloes form earlier in high-density regions and are thus more concentrated than those forming in the field. This impression is strengthened by Fig. 26, which shows the evolution of the 'concentration' $v_{\rm peak}/r_{\rm peak}$ (the symbols are as in Fig. 25). The points on the left are for the haloes forming near the centre (A and C), those on the right for haloes forming in the periphery (B, E, F); the intermediate case D is duely in the middle. Although the ratios change, the two groups are clearly separated at both epochs with higher values of concentration for the former and lower values for the latter group. Recently, Lemson & Kauffmann (1997) have studied correlations between halo properties and local environment using large N-body simulations. Except for the mass distribution of haloes, they do not find any such correlation. It should be noted however that their definition of *locality* is based on a scale of $5–10\,h^{-1}$ Mpc, which is still mildly non-linear today. The correlation we find seems to involve scales of a few Mpc that become non-linear at early epochs. It will be interesting to examine the significance of our result with larger samples of cluster haloes within simulations of even higher resolution.

5.2.2 *Analytic fits*

The evolved density profiles of isolated haloes in N-body simulations are well described for a large range of masses by the analytic model of NFW [although increasing the numerical resolution causes steeper inner profiles, Moore et al. (1998); this is not an issue here since our sample of haloes have similar resolution to those in the NFW simulations]:

$$\frac{\rho(r)}{\rho_{\rm cr}} = \frac{\delta_{\rm c}}{(cr/r_{200})(1 + cr/r_{200})^2}, \tag{1}$$

$$\text{with} \quad \delta_{\rm c} = \frac{200}{3}\frac{c^3}{[\ln(1+c) - c/(1+c)]}. \tag{2}$$

Navarro, Frenk & White (1997) developed an analytic procedure that gives c as a function of the halo mass M_{200} in any hierarchical cosmological model, based on the expected redshift of collapse of a density perturbation of mass M in the Press–Schechter (Press & Schechter 1974) formalism. Here we address the following two questions.

(i) Do the NFW profile and predicted c provide a good description of the profiles of our *peripheral haloes*? As mentioned previously, this question is not trivial since the environment within which these haloes evolved is perturbed by the intense gravitational field of the cluster.

(ii) How much do the tidally stripped *cluster haloes* depart from the NFW predictions ? For example, a steeper outer slope may be typical of these haloes. For this reason, we also consider the Hernquist profile (Hernquist 1990; HER in the following):

$$\frac{\rho(r)}{\rho_{\rm cr}} = \frac{\delta_{\rm c}}{(cr/r_{200})(1 + cr/r_{200})^3}, \tag{3}$$

$$\text{with} \quad \delta_{\rm c} = \frac{400}{3}c(1+c)^2. \tag{4}$$

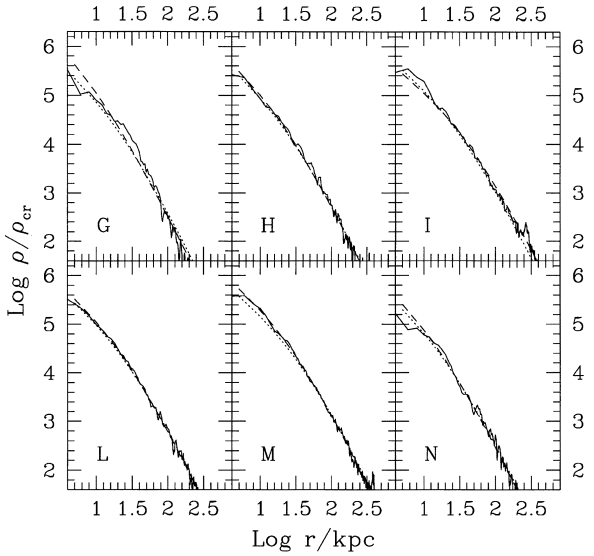

Figure 27. Comparison between the density profiles (at $z = 0$) of a sample of peripheral haloes (solid lines) and the NFW model: the dotted lines are the expected NFW profiles (from halo virial masses) and the dashed lines are fits of the NFW profile to the data.

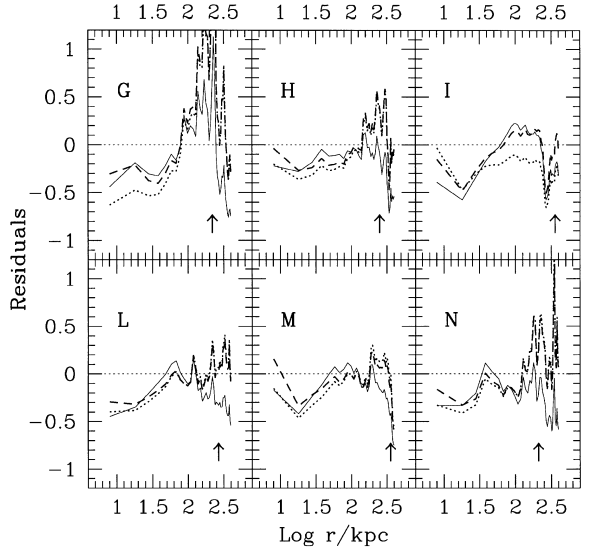

Figure 28. Residuals $[\rho_{\rm NFW}(r) - \rho(r)]/\rho(r)$ between the NFW profiles and density profiles of Fig. 27 (dotted and dashed lines are again for the expected and fitted NFW profiles). The residuals of fits of the Hernquist profile to the data are shown as thin solid lines. The arrows mark the halo virial radii. (For clarity, we show 1 data point every 5.)

This profile has the same inner form as NFW, but asymptotes to r^{-4} on large scales instead of r^{-3}.

First we consider the sample of large *peripheral haloes* described above. Fig. 27 shows their density profiles $\rho(r)/\rho_{0,\rm cr}$. In each panel, the *dotted* and *dashed* lines are NFW profiles *predicted* using the measured M_{200} according to the NFW procedure mentioned above, and *fitted* to the data using a standard χ^2 minimization technique with c as free parameter (using r_{200} measured from the data); for the fits, we used the points in the radial range delimited by $l_{\rm soft}$ and r_{200}. (Two-parameter fits, with both c and r_{200} as free parameters, yield very similar results; we use two-parameter fits for the cluster haloes below, since r_{200} cannot be defined for them.) We plot the residuals

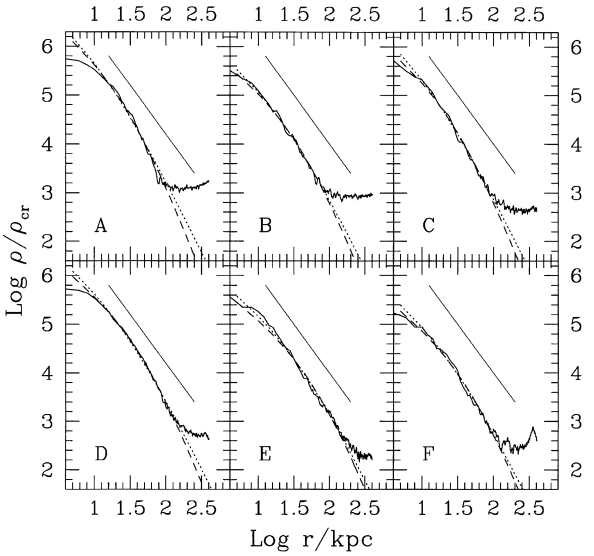

Figure 29. Comparison between the density profiles (at $z = 0$) of a sample of cluster haloes (solid lines) and fits of NFW (dotted lines) and Hernquist's (dashed lines) profiles. An arbitrary isothermal profile is drawn for comparison (thin solid line).

between the data and the NFW profiles and Hernquist profiles in Fig. 28. Each panel shows the fractional difference $[\rho_{\rm model}(r) - \rho(r)]/\rho(r)$ as a function of r, where $\rho(r)$ are the data and $\rho_{\rm model}(r)$ is the density corresponding to one of the analytic profiles considered. With the exception of halo G, the residuals for the NFW profiles are within ∼20–30 per cent at distances from the halo centres $r \gtrsim 15$ kpc. At smaller distances, the profiles of our haloes are steeper than the NFW curves with residuals typically in excess of 30 per cent for the fits and 40 per cent for the predicted curves. Note that, for the same halo, the different NFW curves have concentrations that can differ by various amounts, typically from $c \sim 13$–14 (expected) to 16–18 (fits). The data do not discriminate significantly between NFW and Hernquist's profiles. Only for halo G, as expected from its steep profile, does the HER fit fare better, although it still has positive residuals of ∼40–50 per cent.

Let us now examine the *cluster haloes*. Their density profiles (again solid lines) are shown in Fig. 29, together with NFW (dotted) and HER (dashed) fits [for the latter, we use the data in the radial range delimited by $l_{\rm soft}$ and the value where $\rho(r)$ flattens approaching $\rho_{\rm bkg}$]. Over the scales of interest, the two fits do not differ significantly and both underestimate the central concentrations of the haloes. As before, this can be seen better by examining the residuals in Fig. 30. At intermediate distances from the halo centres ($r \lesssim 40$ kpc), both fits have negative residuals in excess of ∼20 per cent, and in excess of ∼30 per cent on smaller scales. At larger distances, up to about 75 per cent of the halo tidal radii, they generally fare well, with residuals well below 20 per cent. The exception is halo A, which has, like halo G, a particularly steep profile: for this halo, HER is still an acceptable fit, while NFW has large residuals, ∼40–50 per cent. When r approaches $r_{\rm tid}$, the fits depart rapidly from the flattening $\rho(r)$, with average residuals at $r_{\rm tid}$ of the order of 30 per cent or more, for NFW, and about 10 per cent higher for HER.

As a general remark to conclude this section, if we limit the halo sample to lie within $r < 3/4 r_{\rm tid}$, Hernquist's fits are better than NFW for the profiles of cluster haloes (or stripped haloes in general), while the latter model fares well for peripheral haloes. Although our resolution is not good enough to address reliably the issue of halo

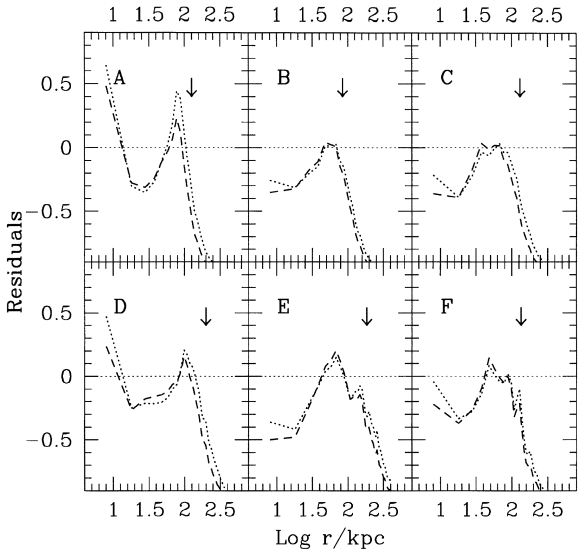

Figure 30. Residuals $[\rho_{\rm FIT}(r) - \rho(r)]/\rho(r)$ for the fits of Fig. 29 (NFW, dotted line, and Hernquist, dashed). The arrows mark the halo tidal radii.

concentrations, it is remarkable that our haloes are systematically more concentrated than the NFW model predicts, when from the poorer resolution we would expect just the opposite. In our analysis, the NFW profiles fitted to the data have concentrations about 25 per cent higher than expected and still they generally underestimate the profiles measured at small scales.

6 SUMMARY AND DISCUSSION

We have explored the consequences of increasing the force and mass resolution within a *dark matter only* simulation of a rich galaxy cluster that forms hierarchically within a cold dark matter simulation of a closed Universe. By resimulating regions of interest using increased resolution, we have attained an unprecedented view of the internal structure of a massive dark halo. With approximately one million particles within the virial radius and force softening that is 0.25 per cent of R_{200}, we resolve 150 haloes with circular velocity larger than 80 $\rm km\,s^{-1}$ within R_{200} at $z = 0$. Most of these haloes have made several orbits within the cluster and are easily identified as potential minima or density enhancements above the background.

This work demonstrates that the loss of dark matter substructure within virialized structures in N-body simulations can be greatly reduced given high enough numerical resolution. The statement that 'at bottom the problem [of overmerging] appears to be not numerical but physical: gravitational dynamics alone cannot explain the existence of galaxy groups and clusters' (Weinberg, Katz and Hernquist 1997) is, in the light of these new results, completely wrong.

Overmerging within the cluster environment is due to the disruption of haloes by the global tidal field and halo–halo encounters (cf. Moore et al. 1996), probably primarily within the large dense haloes prior to the formation of the main cluster. Although our softening length (5 kpc) is a small fraction of the virial radius of the cluster, the rotation curves of the haloes peak at radii of ∼30 kpc. Hence the cores of these haloes can be softened to a degree that effects their evolution. This is the primary reason the haloes are still being disrupted; given high enough force and mass resolution, it should be possible to overcome *most* of the overmerging problems within CDM simulations. An additional loss of substructure can be the result of similar-mass mergers, which is a physical effect, although it is enhanced by poor numerical resolution.

The aim of this paper has been to analyse the properties and dynamics of the dark matter substructure and we find the following key results.

(i) The orbital distribution of substructure haloes is close to that of an isotropic population of tracers in an isothermal potential; the median value of apocentric to pericentric distances is 6:1, a value that does not vary with position within the cluster and is unbiased with respect to the orbits of the smooth particle background. Circular orbits are rare and about 20 per cent of all our surviving haloes within the cluster will pass within 200 kpc $\equiv 0.1R_{200}$.

(ii) Most dark haloes are tidally truncated to a value determined by the (average) density of the cluster at their pericentric positions. The approximation of isothermal halo mass distributions orbiting within a deeper isothermal potential works very well; i.e. $r_{\rm tidal} \sim r_{\rm peri}\sigma_{\rm haloes}/\sigma_{\rm clus}$ (to the level of the accuracy with which we resolve our cluster haloes, that is ∼300–400 particles for most of them).

(iii) The mass attached to dark matter haloes is approximately 13 per cent of the entire cluster mass and varies from nearly 0 per cent within ∼200 kpc from the cluster centre to 20 per cent at its virial radius. This latter value is roughly the expected value for the mass attached to haloes above a circular velocity of 80 $\rm km\,s^{-1}$. Correspondingly, the sizes of haloes vary with clustercentric radius, an effect that may be observable using gravitational lensing of background galaxies.

(iv) Overmerging within the central regions of dense haloes leads to a final distribution of substructure that is antibiased (less centrally concentrated) with respect to the global mass distribution.

(v) The density profiles of a sample of well resolved haloes indicate that those forming in the high-density regions of the collapsing cluster have higher concentrations than those found in isolated environments. We show that this is most probably due to their earlier collapse redshifts rather than the internal response of the haloes to mass loss and heating from tides.

(vi) Most of the haloes within the cluster and in the cluster proximity have density profiles that are well fitted by NFW profiles (Navarro et al. 1996). Halos that lose a great deal of mass through tidal stripping have outer density profiles as steep as $\rho(r) \propto r^{-4}$ (at ≈30 *percent* of their virial radius), thus Hernquist profiles (Hernquist 1990) provide slightly better fits.

(vii) Mergers between haloes in the cluster proximity occur with a frequency of about 5–10 per cent since $z = 0.5$. In the cluster environment mergers are rare; not a single merger occurs for haloes the orbits of which are contained within 1.6 Mpc ≡ 80 per cent R_{200} from the cluster centre.

ACKNOWLEDGMENTS

We would like to thank R. Carlberg, A. Jenkins, J. Navarro, G. Tormen and S. White for interesting discussions. We also thank Neal Katz for helping set up and run the first 'Virgo' cluster simulation and the referee for comments that helped clarify the paper. SG was supported by the University of Milano. BM is supported by the Royal Society. FG acknowledges a fellowship from the EU network for Galaxy Formation and Evolution. We are grateful to Paolo Tozzi and Julio F. Navarro for kindly supplying FORTRAN routines. The numerical simulations were carried out at the Denali Arctic Supercomputing Centre, the IBM SP-2 at the Cornell Theory Center, and on the Cray T3E at the Pittsburgh

Supercomputing Center with support from an NSF Metacentre grant.

REFERENCES

Bahcall N. A., Fan X., Cen R., 1997, ApJ, 485, L53
Bartelmann M., Huss A., Colberg J. M., Jenkins A., Pearce F., 1998, A&A, 330, 1
Borgani S., Da Costa L. N., Freudling W., Giovanelli R., Haynes M. P., Salzer G., Wegner L., 1997a, ApJ, 482, L121
Borgani S., Gardini A., Girardi M., Gottlöber S., 1997b, New. Astron., 2, 119
Brainerd T. G., Goldberg D. M., Villumsen J. V., 1998, ApJ, 502, 505
Butcher H. R., Oemler A., Jr, 1978, ApJ, 226, 559
Butcher H. R., Oemler A., Jr, 1984, ApJ, 285, 426
Carlberg R. G., 1994, ApJ, 433, 468
Carlberg R. G., Dubinski J., 1991, ApJ, 369, 13
Carlberg R. G., Yee H. K. C., Ellingson E., Abraham R., Gravel. P., Morris S., Pritchet C. J., 1996, ApJ, 462, 32
Carlberg R. G., Yee H. K. C., Ellingson E., 1997a, ApJ, 478, 462
Carlberg R. G. et al., 1997b, ApJ, 485, L13
Cen R., 1997, ApJ, 485, 39
Couch W. J., Ellis R. S., Sharples R. M., Smail I., 1994, ApJ 430, 121
Eke V. R., Cole S., Frenk C. S., 1996, MNRAS, 282, 263
Eke V. R., Navarro J. F., & Frenk C. S., 1997, ApJ, in press preprint (astro-ph 9708070)
Evrard A. E., 1997, MNRAS, 292, 289
Evrard A. E., Summers F. J., Davis M., 1994. ApJ, 422, 11
Frenk C. S., Evrard A. E., White S. D. M., Summers F. J. 1996, ApJ, 472, 460
Geiger B., Schneider P., 1998, MNRAS, 295, 497
Gelb J. M., Bertschinger E., 1994, ApJ, 436, 467
Hernquist L., 1990, ApJ, 356, 359
Katz N., Quinn T., Bertschinger E., Gelb J. M., 1994, MNRAS, 270, 71
Klypin A., Gottlöber S., Kravtsov A., 1997, ApJ, submitted (astro-ph/9708191)
Lacey C., Cole S., 1993, MNRAS, 262, 627
Lemson G., Kauffmann G., 1997, MNRAS, submitted (astro-ph/9710125)
Moore B., Katz N., Lake G., 1996, 456, 455
Moore B., Governato F., Quinn T., Stadel J., Lake G., 1998, ApJ, 499, 5
Natarajan P., Kneibb J. P., Smail I., Ellis R. S., 1998, ApJ, 499, 600
Navarro J. F., Frenk C. S., White S. D. M., 1996, ApJ, 462, 563
Navarro J. F., Frenk C. S., White S. D. M., 1997, ApJ, 490, 493
Press W. H., Schecter P., 1974, ApJ, 187, 425
Quinn T., Katz N., Stadel J., Lake G., 1997, preprint (astro-ph 9710043)
Rosati P., Ceca C. R., Norman C., Giacconi R., 1998, ApJ, 492, L21
Smail I., Ellis R. S., Dressler A., Couch W. J., Oemler A., Jr, Sharpless R. M., Butcher H., 1997, ApJ, 479, 70
Summers F. J., Davis M., Evrard A. E., 1995, ApJ, 454, 1
Syer D., White S. D. M., 1997, MNRAS, 293, 337
Tormen G., 1997, MNRAS, 290, 411
Tormen G., Diaferio A., Syer D., 1998, MNRAS, submitted (astro-ph/9712222)
Weinberg D. H., Katz N., Hernquist L., 1997, in Shull J. M., Woodward C. E., Thronson H., eds, ASP Conf. Ser., Origins, in press (astro-ph 9708213)
White S. D. M., Davis M., Efstathiou G., Frenk C. S., 1987, Nat, 330, 451
White S. D. M., Navarro J. F., Evrard A. E., Frenk C. S., 1993, Nat, 366, 429
Wilson G., Cole S., Frenk C. S., 1996, MNRAS, 282, 501
Wu X.-P., Fang L.-Z. H. I., 1997, ApJ 483, 62

This paper has been typeset from a TEX/LATEX file prepared by the author.